

# Magnetic Field Design in a Cylindrical High Permeability Shield: The Combination of Simple Building Blocks and a Genetic Algorithm

M. Packer<sup>1</sup>, P. J. Hobson<sup>1</sup>, A. Davis<sup>1</sup>, N. Holmes<sup>1,2</sup>, J. Leggett<sup>1,2</sup>, P. Glover<sup>1,2</sup>, M. J. Brookes<sup>1,2</sup>, R. Bowtell<sup>1,2</sup>, and T. M. Fromhold<sup>1</sup>

<sup>1</sup>*School of Physics and Astronomy, University of Nottingham, Nottingham, NG7 2RD, UK.*

<sup>2</sup>*Sir Peter Mansfield Imaging Centre, University of Nottingham, Nottingham, NG7 2RD, UK.*

(Dated: 11 March 2022)

Magnetically-sensitive experiments and newly-developed quantum technologies with integrated high-permeability magnetic shields require increasing control of their magnetic field environment and reductions in size, weight, power and cost. However, magnetic fields generated by active components are distorted by high-permeability magnetic shielding, particularly when they are close to the shield's surface. Here, we present an efficient design methodology for creating desired static magnetic field profiles by using discrete coils electromagnetically-coupled to a cylindrical passive magnetic shield. We utilize a modified Green's function solution that accounts for the interior boundary conditions on a closed finite-length high-permeability cylindrical magnetic shield, and determine simplified expressions when a cylindrical coil approaches the interior surface of the shield. We use simple discrete building blocks to provide a complete discrete coil basis to generate any physically-attainable magnetic field in free space. We then use a genetic algorithm to find optimized discrete coil structures composed of this basis. We use our methodology to generate an improved linear axial gradient field,  $dB_z/dz$ , and transverse bias field,  $B_x$ . These optimized structures increase, by a factor of seven and three compared to the standard configurations, the volume in which the desired and achieved fields agree within 1% accuracy, respectively. This coil design method can be used to optimize active-passive magnetic field shaping systems that are compact and simple to manufacture, enabling accurate magnetic field control in spatially-confined experiments at low cost.

## I. INTRODUCTION

The mathematical framework for magnetic field design was first formalized by Romeo and Hoult, who used discrete loops and arcs as the building blocks of a coil basis to generate accurate fields for MRI shimming coils<sup>1</sup>. These magnetic field profiles produced by these simple coil building blocks were expanded in a spherical harmonic basis and the harmonic fields related to the geometry, position, and current of the coil basis elements. The geometries were selected, and their positions adjusted, to minimize unwanted signals and, therefore, maximize the fidelity of a desired magnetic field profile. It was subsequently found that inverse methods based on a continuum representation of the current density could allow the design of higher-fidelity magnetic fields, albeit with more computational effort. Pissanetzky first formulated arbitrary current densities on triangular boundary elements<sup>2</sup>, allowing optimal designs to be found through an entirely numerical method. This formulation was later improved upon by Poole<sup>3</sup>, enabling the flexible design of MRI gradient coils on surfaces of arbitrary geometry using sophisticated 3D-contouring methods. Pseudo-analytical techniques have also been developed on specific surface geometries using Green's function expansions and quadratic optimization methods that enable the rapid design of accurate user-specified magnetic fields in free space<sup>4-7</sup>.

Newly-developed quantum technologies with greater performance and reduced size have further increased the demand for state-of-the-art magnetically-controlled environments. The applications of these technologies range from fundamental physics experiments<sup>8-13</sup> to biomedical imaging<sup>18-25</sup>. Magnetic field control is required in many of these technologies to trap and manipulate atoms. To translate these laboratory experiments to usable devices in real-world settings, high-permeability passive magnetic shields are used to attenuate stray magnetic fields caused by nearby electronic equipment and/or the local Earth's magnetic field. Specifically, cylindrical and cubic magnetic shields are often used in these systems as they are simple to manufacture, provide good shielding, and can accommodate equipment easily inside them<sup>26-28</sup>. However, previous longstanding methods of magnetic field design do not incorporate the interaction of active current-carrying coils with the high-permeability passive shielding materials. Consequently, if these methods are used to design coils to generate specific magnetic fields in shielded environments, the magnetic shield will distort the field profile, prohibiting the desired level of field control<sup>29</sup>.

Motivated by this problem, several novel numerical and analytical methods have recently been developed that incorporate high-permeability passive shielding material into their design methodologies. The numerical methods use

an equipotential scalar field to enforce the boundary condition on the shield's surface, and then account for this in the design of surface currents using boundary elements on arbitrary geometries inside the shield<sup>30,31</sup>. The analytical methods rely on modifying the Green's function to satisfy the boundary condition on the shield's surface. The currents are then decomposed into an orthogonal basis set where the magnetic fields generated by the combined system can be calculated<sup>32,33</sup>. These methods can design complex current distributions that generate extremely accurate magnetic fields inside shielded environments. However, to realize these high fidelity fields physically, the designs must be carefully discretized and accurately represented in real systems. In many of these systems, magnetic field control is not the only area of concern. Optical access, miniaturization, and cost also constrain the development of many of these technologies. Consequently, field design methods in shielded environments must accommodate these additional constraints. In this context, using optimally-placed discrete coil designs could allow for simplistic, cost-effective, and accurate generation of magnetic fields with greater optical access at a much lower cost. Some simple discrete coil geometries have been formulated that allow the design optimization of magnetic field-generating systems in shielded environments. However, these are restricted to circular loops and simple transverse fields<sup>34-37</sup>. Currently, no generalized discrete coil optimization method exists that incorporates the interaction with high-permeability shielding; partly due to the multitude of free parameters associated with discrete coils and their complex electromagnetic interaction with an exterior magnetic shield.

Alongside this, multi-objective optimization procedures, such as genetic algorithms, particle swarm optimizations, and differential evolution algorithms, have garnered considerable attention over the past decade because of their ability to find optimal solutions to complicated problems with mixed constraints<sup>38,39</sup>. Advances in computational power and code accessibility have made these algorithms much easier to implement<sup>40</sup>. In this paper, using the analytical formulation of cylindrical coils in a cylindrical magnetic shield<sup>32</sup>, the framework of Romeo and Hault<sup>1</sup>, and a genetic algorithm optimization procedure<sup>41</sup>, we present a widely-applicable design methodology that enables the construction of optimized discrete coils in cylindrical magnetic shields. Firstly, we expand on the analytical formulation by determining an approximate form of the magnetic field when the coil is close to the surface of the magnetic shield. Secondly, we formulate a complete coil basis in cylindrical coordinates that allows the simple construction of harmonic fields using discrete coils. Finally, we find optimal configurations of multiple nested sets of the discrete coil basis to generate specified harmonic fields utilizing a genetic algorithm. By incorporating these different elements, our method enables the simple design of specified magnetic field profiles in high-permeability cylindrical magnetic shields constrained by optical access, cost, and size, thereby enabling the miniaturization and commercialization of technologies that require precisely-controlled magnetic field environments.

## II. MODEL

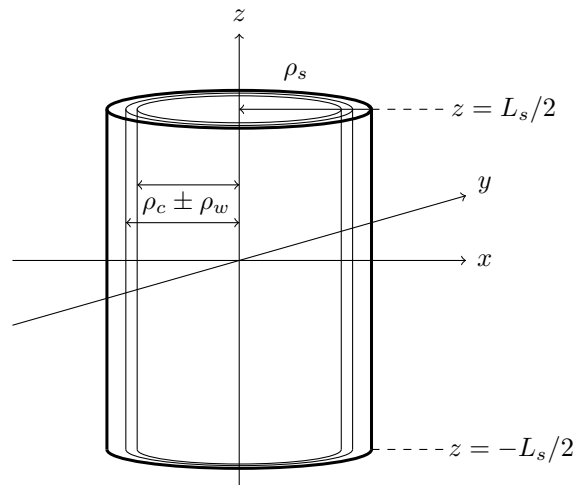


FIG. 1: Cylindrical magnetic shield with high permeability,  $\mu_r \gg 1$ , of length  $L_s$  and inner radius  $\rho_s$  with planar end caps located at  $z = \pm L_s/2$ . A coil of radius  $\rho_c$  and equal length to the shield is placed symmetrically inside the shield, and the coils are formed of wire of radius  $\rho_w$ .

Here, we consider a closed high-permeability cylinder of inner radius  $\rho_s$  and length  $L_s$ , with planar end caps located at  $z = \pm L_s/2$ . Inside this cylinder, a current,  $\mathbf{J}$ , flows on a co-axially nested cylindrical surface of radius  $\rho_c$ , thickness

$2\rho_w$ , and length  $L_s$ , as shown in Fig. 1, such that  $\rho_c + \rho_w \leq \rho_s$ . We wish to solve for the relation between the optimal current flow and the field generated inside the coil and shield. Within previous works<sup>32,33</sup> Green's function solutions to similar problems have been formulated that satisfied the interface conditions

$$\left(\frac{1}{\mu_r}\mathbf{B}_{\text{mat.}} - \mathbf{B}_{\text{air}}\right) \wedge \hat{\mathbf{n}} = 0 \quad \text{on } S, \quad (1)$$

and

$$(\mathbf{B}_{\text{mat.}} - \mathbf{B}_{\text{air}}) \cdot \hat{\mathbf{n}} = 0 \quad \text{on } S, \quad (2)$$

at the surface  $S$  of a high permeability cylindrical magnetic shield, where  $\hat{\mathbf{n}}$  is the unit vector normal to  $S$  and  $\mu_r$  is the relative permeability of the shielding material. This was achieved by casting the induced magnetization of the shield into a mathematically-equivalent surface pseudo-current,  $\nabla \wedge \mathbf{M} = \tilde{\mathbf{J}}$ , which can then be related to the vector potential,  $\mathbf{B} = \nabla \wedge \mathbf{A}$ , to generate the Poisson equation,

$$\nabla^2 \mathbf{A} = -\mu_0(\mathbf{J} + \tilde{\mathbf{J}}). \quad (3)$$

In the high-permeability regime, the boundary conditions at the shield's surface can be approximated as

$$B_\rho \Big|_{z=\pm L_s/2} = 0, \quad B_\phi \Big|_{z=\pm L_s/2, \rho=\rho_s} = 0, \quad B_z \Big|_{\rho=\rho_s} = 0. \quad (4)$$

Previously<sup>32</sup>, the Green's function solution for Poisson's equation, (3), is formulated using the surface pseudo-current to satisfy the boundary condition, (4), over the interior surface of the magnetic shield. The radial boundary condition is satisfied by equating the magnetic field generated by an arbitrary cylindrical current and pseudo-current on the surface of a shield of infinite length at  $\rho = \rho_s$ . The boundary conditions on the end caps can then be satisfied by using the method of mirror images<sup>43</sup> to generate images of the current and pseudo-current. Due to the orthogonality of the planar end caps, the reflected image currents continue to satisfy the radial boundary condition, therefore satisfying the boundary condition over the entire domain of the magnetic shield. The total field, in a region within the cylinder  $\rho < \rho_c$ , is then given by<sup>32</sup>

$$B_\rho(\rho, \phi, z) = \frac{i\mu_0\rho_c}{2\pi} \sum_{m=-\infty}^{\infty} \sum_{p=-\infty}^{\infty} \int_{-\infty}^{\infty} dk \, k e^{im\phi} e^{ikz} I'_m(|k|\rho) R_m(k, \rho_c, \rho_s) J_\phi^{mp}(k), \quad (5)$$

$$B_\phi(\rho, \phi, z) = -\frac{\mu_0\rho_c}{2\pi\rho} \sum_{m=-\infty}^{\infty} \sum_{p=-\infty}^{\infty} \int_{-\infty}^{\infty} dk \, m \frac{|k|}{k} e^{im\phi} e^{ikz} I_m(|k|\rho) R_m(k, \rho_c, \rho_s) J_\phi^{mp}(k), \quad (6)$$

$$B_z(\rho, \phi, z) = -\frac{\mu_0\rho_c}{2\pi} \sum_{m=-\infty}^{\infty} \sum_{p=-\infty}^{\infty} \int_{-\infty}^{\infty} dk \, |k| e^{im\phi} e^{ikz} I_m(|k|\rho) R_m(k, \rho_c, \rho_s) J_\phi^{mp}(k), \quad (7)$$

where  $R_m(k, \rho_c, \rho_s) = K'_m(|k|\rho_c) - I'_m(|k|\rho_c)K_m(|k|\rho_s)/I_m(|k|\rho_s)$ , and  $J_\phi^{mp}(k)$  is the Fourier transform with respect to  $z$  and  $\phi$  of the  $p^{\text{th}}$  reflected image current determined via the method of mirror images, where the  $p = 0$  term represents the Fourier transform of the actual current distribution which is confined to the region  $|z'| < L_s/2$

$$J_\phi^{mp}(k) = \frac{1}{2\pi} \int_0^{2\pi} d\phi' \, e^{-im\phi'} \int_{-\infty}^{\infty} dz' \, e^{-ikz'} J_\phi(\phi', (-1)^p(z' + pL_s)), \quad (8)$$

where  $(\phi', z')$  specify position on the current-carrying surface.

Previously, this formulation has been used to design coils through a harmonic minimization method with a continuum representation of the current. The optimal continuum solution can be found using a quadratic programming algorithm wherein the continuum solution is discretized into a physical wire pattern that approximates the continuous current distribution. The errors introduced in this method result either from assuming that the shield is a perfect magnetic conductor, which does not saturate, or from inaccurately discretizing the current continuum such that both the coil and,

consequently, the magnetic shield introduce erroneous fields. For most real-world applications, the perfect magnetic conductor approximation introduces extremely small errors that are far less significant than the errors introduced during manufacturing. For example, assuming  $\mu_r > 20000$  and material thickness  $d_s = 1$  mm, the typical deviation from the analytical solution is  $< 0.005\%$ <sup>32,44,45</sup>. Furthermore, high-grade annealed cylindrical mumetal shields have been experimentally shown to effectively shunt internal fields up to  $H = 40$  A/m before complete saturation<sup>42</sup>, which is more than enough for the micro-Tesla field applications required for the majority of shielded experiments. Therefore, in many systems, the dominant error is generated by discretization of the current continuum, which is hard to quantify *a priori* as it is design dependent. The discretization error can only be alleviated by better representing the current continuum with a higher wire density. Although technologies like flex-PCBs<sup>46</sup> and 3D-printers<sup>47</sup> offer the capability to represent the continuum very accurately, such coils are expensive, time-consuming to manufacture, and hard to repair if there is a breakage. Moreover, the required wire positions and high wire density may block experimental access to the interior of the shield. Thus, it follows that applying a formulation to design fields using simple discrete coils that are robust and easy to manufacture will benefit numerous experimental systems.

To maximize the available interior volume of the system, as is normally required for real-world applications, we consider discrete coils that are positioned at the shield's inner surface,  $\rho_c = \rho_s - \rho_w$ , and determine their parameters using forward numerical optimization techniques, thereby circumventing discretization error entirely. When the coil is pressed against the inner surface of the shield, we can expand the magnetic field as a power series of the (small) wire radius such that

$$\mathbf{B}(\rho, \phi, z) = \mathbf{B}^0(\rho, \phi, z) + \rho_w \mathbf{B}^1(\rho, \phi, z) + \rho_w^2 \mathbf{B}^2(\rho, \phi, z) + \dots, \quad (9)$$

where the  $\mathbf{B}^\nu$  terms are  $\nu^{\text{th}}$  order field perturbations for  $\nu \in \mathbb{Z}^{0+}$ . If the radius of wire is sufficiently small compared to the radius of the magnetic shield, the magnetic field can be approximated while only introducing small deviations. Here, we give the example of a simple loop placed at the center of a shield with aspect ratio  $L_s/(2\rho_s) = 1$  and wire radii  $\rho_w < 0.01\rho_s$ . The error between the zeroth-order term and the complete solution is less than 0.06% at the center, as shown by Fig. 2, but, moving away from the origin, this error increases dramatically. This increase is due to a zero in the axial field caused by the magnetic shield's interaction, disproportionately skewing the error. Discounting this region, the error within a radial position  $\rho < 0.8\rho_s$  is less than 0.5%. Henceforth, in this paper, we assume that  $\rho_w < 0.01\rho_s$  and use only the zeroth-order term to design coils in this regime. The magnetic field components are then approximated, through the use of the Wronskian, resulting in the governing equations

$$B_\rho(\rho, \phi, z) = -\frac{i\mu_0}{2\pi} \sum_{m=-\infty}^{\infty} \sum_{p=-\infty}^{\infty} \int_{-\infty}^{\infty} dk \frac{k}{|k|} e^{im\phi} e^{ikz} \frac{I'_m(|k|\rho)}{I_m(|k|\rho_s)} J_\phi^{mp}(k), \quad (10)$$

$$B_\phi(\rho, \phi, z) = \frac{\mu_0}{2\pi\rho} \sum_{m=-\infty}^{\infty} \sum_{p=-\infty}^{\infty} \int_{-\infty}^{\infty} dk \frac{m}{k} e^{im\phi} e^{ikz} \frac{I_m(|k|\rho)}{I_m(|k|\rho_s)} J_\phi^{mp}(k), \quad (11)$$

$$B_z(\rho, \phi, z) = \frac{\mu_0}{2\pi} \sum_{m=-\infty}^{\infty} \sum_{p=-\infty}^{\infty} \int_{-\infty}^{\infty} dk e^{im\phi} e^{ikz} \frac{I_m(|k|\rho)}{I_m(|k|\rho_s)} J_\phi^{mp}(k). \quad (12)$$

For a set-up where the  $\rho_w > 0.01\rho_s$ , the validity of the approximation should be determined for each individual scenario and adjusted appropriately for a given field design tolerance and experimental system.

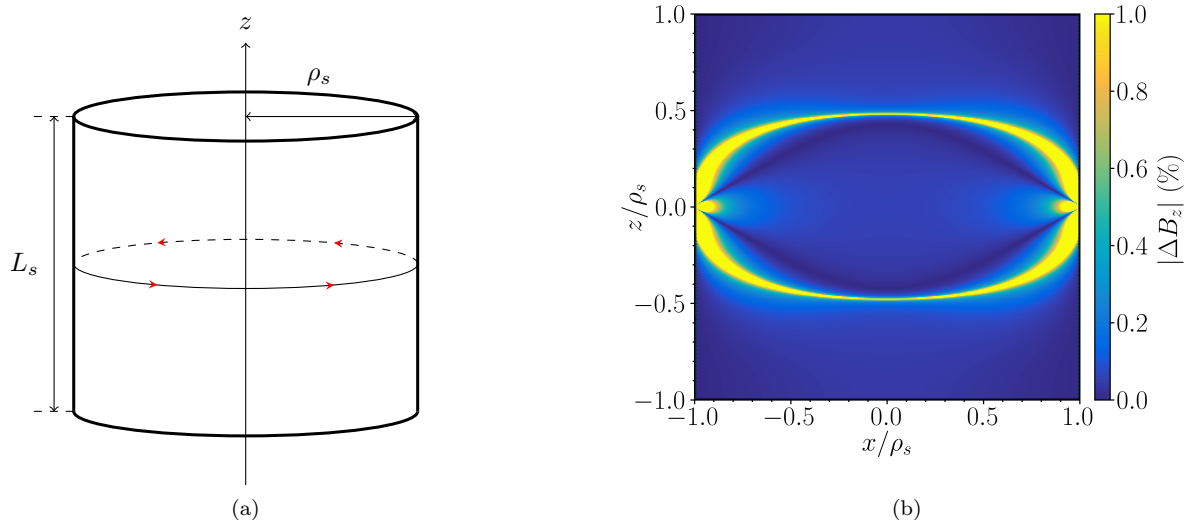


FIG. 2: (a) Schematic diagram of a loop of radius  $\rho_s$  at position  $z = 0$  in a closed magnetic shield of radius  $\rho_s$  and length  $L_s = 2\rho_s$ . (b) Color map showing the absolute error,  $|\Delta B_z|$ , between the axial zeroth-order contribution in (12) and the exact solution in (7) for the example depicted in (a).

### III. COIL BASIS

Decomposing the magnetic field into a complete set of orthogonal eigenfunctions, with associated eigenvalues, allows the desired field profile to be selected while minimizing erroneous contributions.

In free space, the magnetic field can be represented as the gradient of a scalar potential,  $\mathbf{B} = -\nabla\Psi$ . The scalar potential and magnetic field, (10)–(12), both satisfy Laplace's equation and can be represented as a sum of orthogonal functions in an orthogonal curvilinear coordinate system. In this work, following Romeo and Hoult<sup>1</sup>, we represent the scalar potential as the set of real spherical harmonics in spherical polar coordinates and, therefore, expand the magnetic field as

$$\mathbf{B}(r, \theta, \phi) = \nabla \sum_{n=0}^{\infty} \sum_{m=-n}^n C_{n,m} r^n P_{n,|m|}(\cos \theta) \begin{pmatrix} \cos(|m|\phi) \\ \sin(|m|\phi) \end{pmatrix}, \quad \begin{matrix} m \geq 0 \\ m < 0 \end{matrix} \quad (13)$$

where the harmonic fields are classified through their order,  $n$ , and degree,  $m$ . Each harmonic has a magnitude,  $C_{n,m}$ , and a  $\theta$  dependence that is described by one of the Ferrer's associated Legendre polynomials,  $P_{n,|m|}(\cos \theta)$ . The harmonics are mutually orthogonal on the surface of a sphere, with high-order  $n$  and  $m$  harmonics representing higher frequency variations in the field along the zenith and azimuthal directions, respectively. Due to their relation with the associated Legendre polynomials, the axial symmetry of the spherical harmonics depends on the parity of  $(n + m)$ . The degree is then divided into two cases,  $m = 0$  and  $|m| > 0$ . The  $m = 0$  harmonic fields exhibit total azimuthal symmetry and are known as zonal harmonics,  $Z_n$ . The  $|m| > 0$  harmonic fields exhibit  $m$ -fold azimuthal symmetry and are known as tesseral harmonics,  $T_{n,m}$ , where negative  $m < 0$  harmonic fields are  $\pi/2|m|$  azimuthal rotations of their positive  $m > 0$  counterparts. Using this basis any magnetic field in free space can be decomposed into a combination of axially odd and even, zonal and tesseral harmonic fields.

Due to the link between the magnetic field and the scalar potential, every vector component of the magnetic field must depend on a single scalar function. However, some scalar fields are not present in every vector component of the magnetic field. This is most clearly seen though the spherical harmonic decomposition of the axial magnetic field component

$$B_z(r, \theta, \phi) = \sum_{n=1}^{\infty} \sum_{m=-n+1}^{n-1} C_{n,m} (n + |m|) r^{n-1} P_{n-1,|m|}(\cos \theta) \begin{pmatrix} \cos(|m|\phi) \\ \sin(|m|\phi) \end{pmatrix}, \quad \begin{matrix} m \geq 0 \\ m < 0 \end{matrix} \quad (14)$$

as derived in Appendix A. Again, due to the symmetry of the associated Legendre polynomials, the axial parity of the axial field is odd if  $(n + m - 1) = 2\nu + 1$ , and even if  $(n + m - 1) = 2\nu$ , respectively, for  $\nu \in \mathbb{Z}$ . Here, no axial field exists where  $n = |m|$ . Although the complete set of harmonic fields do not exist within the axial field, any harmonic can be indirectly selected using it. This requires the correct current density basis to be chosen such that the harmonics that are not present in the axial field can be removed independently. Here, we consider the appropriate cylindrical basis for discrete current loops placed symmetrically inside a cylindrical magnetic shield, i.e. the basis that enables the most efficient construction of the complete set of harmonic fields using only the axial field. It should be noted that this could be performed with any vector component of the magnetic field. However, using any other component is more complicated<sup>1</sup>.

As the axial magnetic field (7) is directly related to the Fourier transform of the azimuthal current density, the axial parity and azimuthal symmetry of the axial field must mirror those of the azimuthal current density. As the current density can be written as a product of two terms - one varying with  $z$  and one varying with  $\phi$ , their variations can be decoupled independently to maximize harmonics with specified  $n$  and  $m$ , respectively. To generate zonal harmonics this requires closed circular current loops with complete azimuthal symmetry. To maximize the strength of a specific tesseral harmonic, an arc with the same azimuthal periodicity as the desired harmonic is needed. Then, to match the axial parity of a desired harmonic field, pairs of axially separated axially symmetric and anti-symmetric loops and arcs are used. These combinations of zonal and tesseral, symmetric and anti-symmetric, pairs constitute the coil basis that will be used to construct any arbitrary harmonic field and, therefore, any physical magnetic field in free space. Additionally, because arcs are not continuous, they must be linked via axial connections, forming saddle-like systems<sup>48</sup>. These axial wires contribute to the off-axis field components but, due to the formulation of the magnetic field, these variations are accounted for and encoded within the azimuthal Fourier transform. Symmetric arc pairs, therefore, require twice the number of axially-separated arcs to ensure current continuity. Hence, these systems must be composed of double saddle Golay-type coils<sup>49</sup>.

For simplicity, we formulate these building blocks centered about the origin, maintaining parity symmetry within the magnetic shield. It must be noted, however, that a formulation can be performed with asymmetric current loop placement, albeit with the added complication of both axially odd and even parity harmonics being present simultaneously.

Let us decompose the current density into axial and azimuthal components

$$J_\phi(\phi', z') = I\Phi(\phi')Z(z'), \quad (15)$$

where  $I$  is the current in the wire. The axial variation of a symmetric or anti-symmetric pair separated by an axial distance  $2d$ , is given by

$$Z^\pm(z') = \delta(z' - d) \pm \delta(z' + d), \quad (16)$$

with the resulting  $p^{\text{th}}$  reflected Fourier transform from (8) written as

$$J_\phi^{mp}(k) = e^{ikpL_s} \left( e^{-(-1)^p ikd} \pm e^{(-1)^p ikd} \right) \Phi^m, \quad (17)$$

where the azimuthal Fourier transform of the azimuthal variation of the current density is

$$\Phi^m = \frac{1}{2\pi} \int_0^{2\pi} d\phi' e^{-im\phi'} \Phi(\phi'). \quad (18)$$

To maximize a specific degree of harmonic,  $m = M$ , with either complete azimuthal symmetry,  $M = 0$ , or periodicity,  $\pi/|M|$ , the azimuthal component is chosen according to the desired harmonic field, given by

$$\Phi(\phi') = \begin{cases} \sum_{\lambda=0}^{2M-1} (-1)^\lambda \left[ H\left(\phi' + \varphi - \frac{\lambda\pi}{M}\right) - H\left(\phi' - \varphi - \frac{\lambda\pi}{M}\right) \right], & M > 0 \\ 1, & M = 0 \\ \sum_{\lambda=0}^{2M-1} (-1)^\lambda \left[ H\left(\phi' + \varphi - \frac{\lambda\pi}{|M|} - \frac{\pi}{2|M|}\right) - H\left(\phi' - \varphi - \frac{\lambda\pi}{|M|} - \frac{\pi}{2|M|}\right) \right], & M < 0 \end{cases} \quad (19)$$

where  $H(x)$  is the Heaviside function. These azimuthal variations are illustrated in Fig. 3. The azimuthal Fourier

transform, from (18), is then found to be

$$\Phi^m(\varphi) = \begin{cases} \frac{\sin(m\varphi)}{\pi m} \sum_{\lambda=0}^{2M-1} (-1)^\lambda e^{-\frac{im\lambda\pi}{M}}, & M > 0 \\ \delta_{m0}, & M = 0 \\ \frac{\sin(m\varphi)}{\pi m} e^{-\frac{im\pi}{2|M|}} \sum_{\lambda=0}^{2|M|-1} (-1)^\lambda e^{-\frac{im\lambda\pi}{|M|}}. & M < 0 \end{cases} \quad (20)$$

Due to the preserved symmetries within the system, axial symmetric and anti-symmetric coils can only generate odd and even parity harmonics, respectively. From this parity, the symmetry of a specific order of harmonic,  $n = N$ , and, subsequently, axial coil symmetry, can then be chosen to select the required field symmetries within the system. These building blocks, composed of zonal and tesseral, symmetric and anti-symmetric, coils are shown in Fig. 4.

Using (17), (15) and (12), and noting that the expression can be written in terms of a Fourier series, the axial magnetic field generated by symmetric and anti-symmetric pairs is given by

$$B_z^\pm(\rho, \phi, z) = \frac{2\mu_0 I}{L_s} \sum_{m=-\infty}^{\infty} b_m^\pm(\rho, z; d) e^{im\phi} \Phi^m, \quad (21)$$

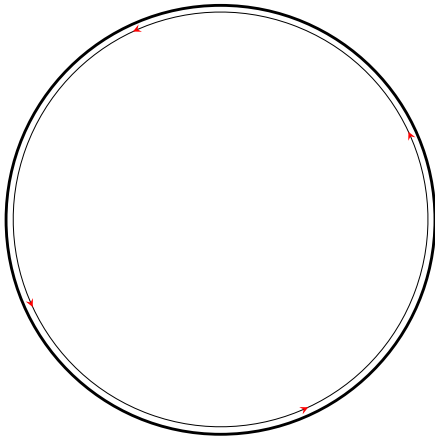
respectively, where

$$b_m^+(\rho, z; d) = \sum_{p \text{ even}} \cos\left(\frac{\pi pz}{L_s}\right) \cos\left(\frac{\pi pd}{L_s}\right) \frac{I_m\left(\left|\frac{\pi p}{L_s}\right|\rho\right)}{I_m\left(\left|\frac{\pi p}{L_s}\right|\rho_s\right)}, \quad (22)$$

$$b_m^-(\rho, z; d) = \sum_{p \text{ odd}} \sin\left(\frac{\pi pz}{L_s}\right) \sin\left(\frac{\pi pd}{L_s}\right) \frac{I_m\left(\left|\frac{\pi p}{L_s}\right|\rho\right)}{I_m\left(\left|\frac{\pi p}{L_s}\right|\rho_s\right)}, \quad (23)$$

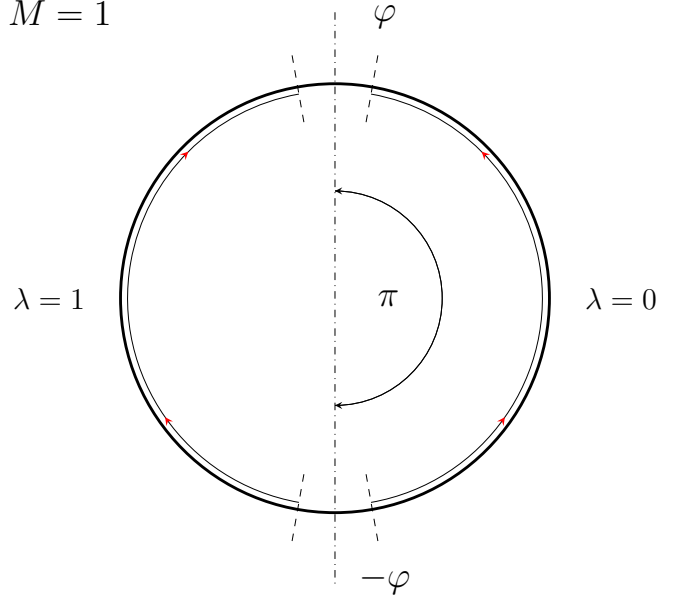
are symmetric and anti-symmetric axial magnetic field variations, respectively, of the coil basis. Using this coil basis that generates zonal and tesseral, symmetric and anti-symmetric, fields we may now begin to construct coil structures that select specific harmonic fields.

Zonal  
 $M = 0$



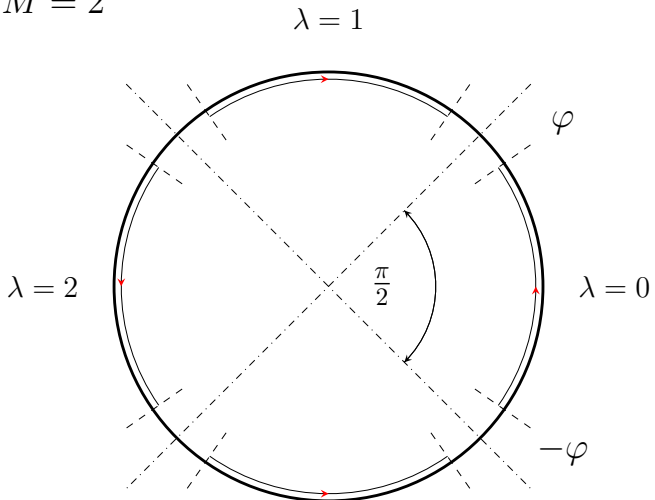
(a)

Tesseral  
 $M = 1$



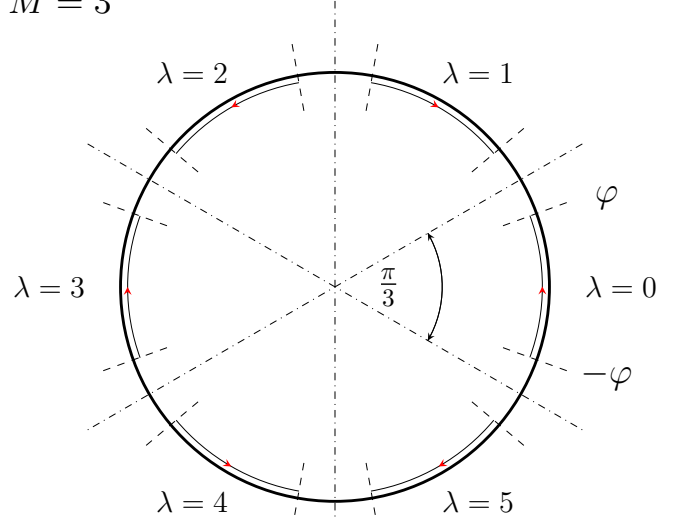
(b)

Tesseral  
 $M = 2$



(c)

Tesseral  
 $M = 3$



(d)

FIG. 3: Azimuthal variation in the basis currents on the  $\rho\phi$ -plane required by (19) to generate (a) the zonal,  $M = 0$ , and (b–d) tesseral harmonics of degree one, two, and three,  $M = (1 - 3)$ , respectively, where the azimuthal arc length for each period,  $\lambda$ , is given by  $2\varphi$ . Red arrow heads show the direction of current flow.

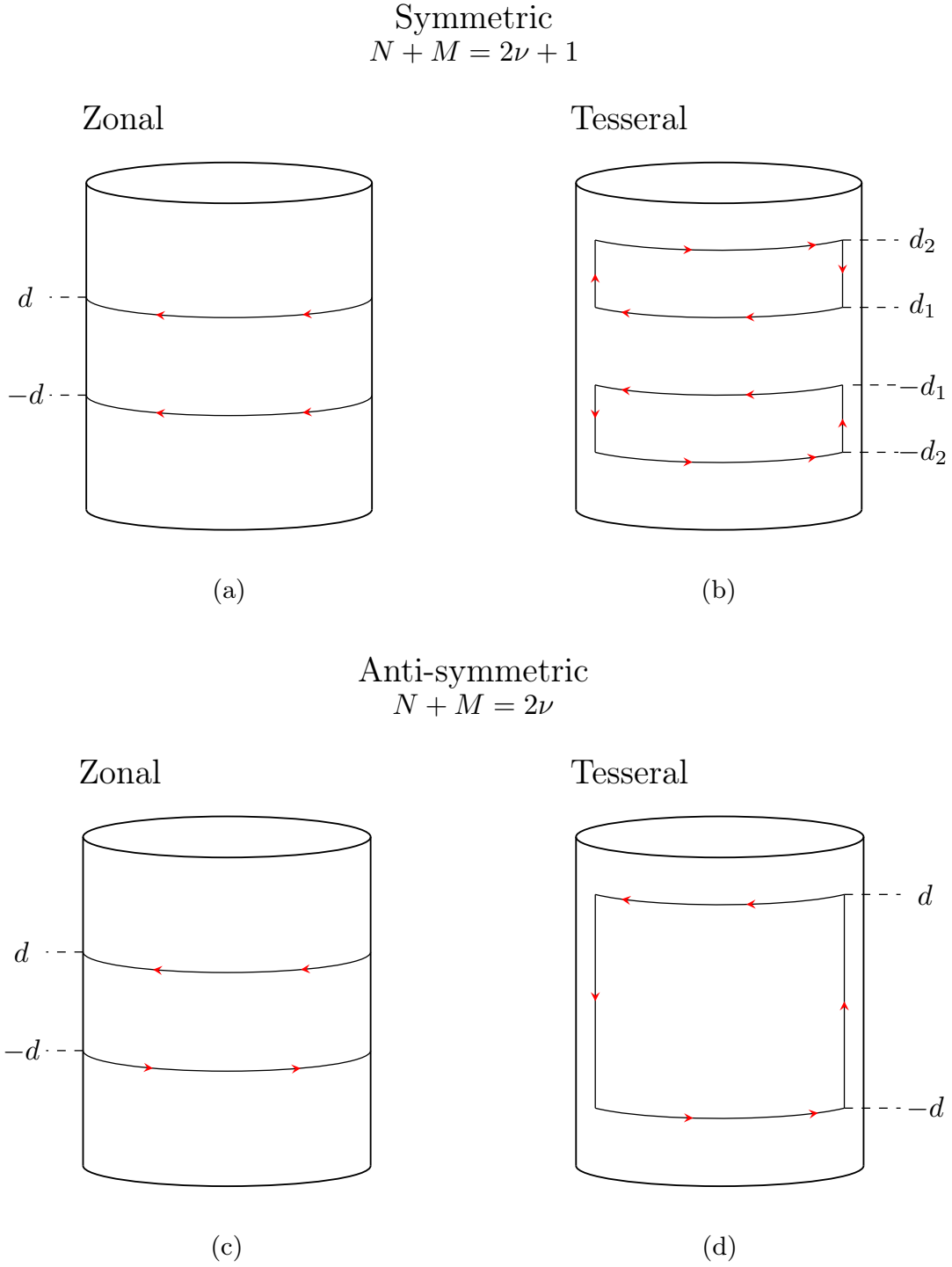


FIG. 4: Azimuthal and axial variation in the basis currents on the  $\phi z$ -plane required by (15) to generate (a)-(b) symmetric,  $(N + M) = 2\nu + 1$ , and (c)-(d) anti-symmetric,  $(N + M) = 2\nu$ , zonal and tesseral harmonics, respectively, where  $N$  and  $M$  are the order and degree of the harmonic and  $\nu \in \mathbb{Z}$ . Red arrow heads show the direction of current flow.

#### IV. HARMONIC SELECTION

The methodology for designing a coil to generate a specific spherical harmonic variation in any vector direction relies on the azimuthal variation and axial symmetries generated by the coil basis and their connection to the axial magnetic and scalar spherical harmonic fields in free space.

The azimuthal variations and, subsequently, the degrees of the harmonics generated, as described in (21), are determined by the periodicity of a given coil configuration. Thus, to maximize the degree of any desired harmonic we must consider the azimuthal Fourier transform, (20). For  $M = 0$ , it is apparent that loops only generate fields of degree  $m = 0$  and, so, do not require azimuthal optimization. For  $|M| > 0$ , however, sets of arcs of periodicity  $\pi/M$  generate an infinite number of harmonic fields of degree  $m = (2\nu + 1)M$ , where  $\nu \in \mathbb{Z}^{0+}$ . Therefore, to maximize the desired degree of a tesseral harmonic field, the angular length,  $\varphi$ , should be adjusted to eliminate as many undesired azimuthal variations as possible. From analysis of (20), the leading-order error term of degree  $m = 3M$  is removed simply if

$$\sin(3M\varphi) = 0. \quad (24)$$

However, depending on the required accuracy of the desired field, further variations might need to be removed. To achieve this, additional arcs of angular length  $\varphi_j$  and azimuthal turn ratios,  $I_j^\varphi$ , can be used to allow multiple degrees to be minimized simultaneously, as shown in Fig. 5a. Hence, generalizing (24), we can use  $M'$  arcs simultaneously to minimize  $\tilde{M}$  degrees of harmonics,

$$\min_{\varphi_j, I_j^\varphi} \left[ \sum_{j=1}^{M'} I_j^\varphi \sin((2\nu + 1)M\varphi_j) \right], \quad \nu \in \mathbb{Z} : \nu \in [1, \tilde{M}]. \quad (25)$$

Therefore, using this relation, the harmonics which do not exist within the axial field,  $m = n$ , can be selected or minimized. In theory, as there are  $2M'$  independent variables,  $2M'$  degrees can be removed from the equations describing the system. For practical applications,  $I_j^\varphi$  must be integer ratios of one-another and connected in series, limiting the space in which optimal  $\varphi_j$  can exist. The equations (25) can be solved analytically for integer  $I_j^\varphi$  by substituting the appropriate Chebyshev polynomials. However, it is often quicker to solve these equations using a numerically exhaustive search technique because the Chebyshev polynomials may be more complex than solutions to equation (25). Typically, the best solutions have significant angular extents and azimuthal turn ratios within an order of magnitude of each other to prevent the finite size of the wires from introducing unwanted deviations from the desired field. It should also be noted that the value of  $I_j^\varphi$  can be negative, meaning that in the  $j^{\text{th}}$  arc, current flows in the opposite direction from when  $I_j^\varphi$  is positive. Designs with counter-propagating current flows are useful if there are specific regions where wires are prohibited, providing additional flexibility when designing coil setups. They are, however, often very power-inefficient.

The same logic can also be applied to the radial and axial field variations to remove harmonics of odd or even parity. To illustrate this, we first transform the spherical harmonic field (14) into cylindrical coordinates, and separate it into terms of even and odd order,

$$B_z = \left[ \sum_{n=0}^{\infty} \sum_{m=-2n}^{2n} C_{2n+1,m} (2n + |m| + 1) (\rho^2 + z^2)^n P_{2n,|m|} \left( \frac{z}{(\rho^2 + z^2)^{1/2}} \right) + \sum_{n=1}^{\infty} \sum_{m=-2n-1}^{2n-1} C_{2n,m} (2n + |m|) (\rho^2 + z^2)^{\frac{n-1}{2}} P_{2n-1,|m|} \left( \frac{z}{(\rho^2 + z^2)^{1/2}} \right) \right] \begin{cases} \cos(|m|\phi) & m \geq 0 \\ \sin(|m|\phi) & m < 0 \end{cases}. \quad (26)$$

After analyzing (26) and (21), we can see that the radial and axial dependence of every harmonic of order  $n$  and degree  $m$ , excluding  $m \neq n$ , must be completely contained within the symmetric and anti-symmetric axial field variations (22)–(23). Therefore, we can write these variations in terms of the harmonic magnitudes

$$b_m^+(\rho, z; d) = \sum_{n=0}^{\infty} \tilde{C}_{2n+1,m}(d, \rho_s, L_s) (\rho^2 + z^2)^n P_{2n,|m|} \left( \frac{z}{(\rho^2 + z^2)^{1/2}} \right), \quad |m| \leq 2n \quad (27)$$

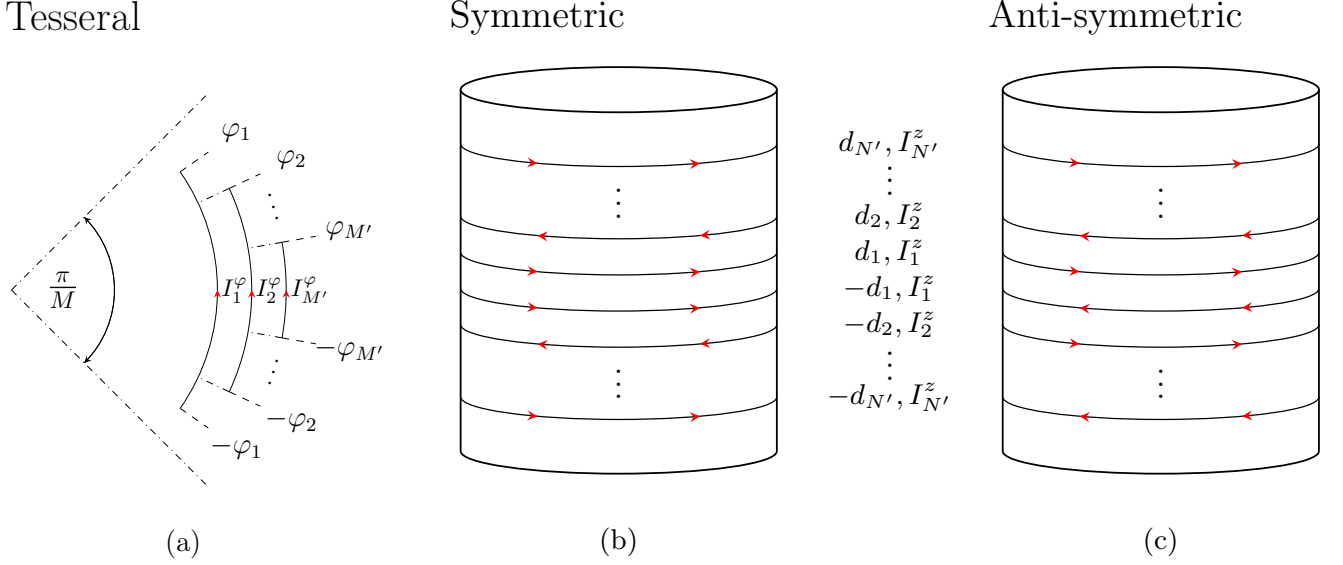


FIG. 5: Sets of the basis currents from (15) to generate more accurate (a) tesseral harmonics of degree  $M$  presented on the  $\rho\phi$ -plane and (b)-(c) symmetric and anti-symmetric zonal harmonics, respectively, presented on the  $\phi z$ -plane, where  $N'$  and  $M'$  are the number of basis currents used. Red arrow heads show the direction of current flow.

$$b_m^-(\rho, z; d) = \sum_{n=1}^{\infty} \tilde{C}_{2n,m}(d, \rho_s, L_s) (\rho^2 + z^2)^{\frac{2n-1}{2}} P_{2n-1,|m|} \left( \frac{z}{(\rho^2 + z^2)^{1/2}} \right), \quad |m| \leq 2n - 1 \quad (28)$$

where  $\tilde{C}_{n,m}(d, \rho_s, L_s)$  describes the effective harmonic magnitude, which depends on the coil and shield parameters. The relationship between  $\tilde{C}_{n,m}(d, \rho_s, L_s)$  and the placement of loops and arcs is apparent when the series expansions of both the trigonometric and Bessel functions are substituted into (22)-(23). The spatial variations can then be separated and grouped into their constituent harmonics then related to the coil parameters. This must be done on a case-by-case basis as only specific sets of harmonics exist within each of the basis coils. Once the harmonics have been separated and effective harmonic magnitudes found in terms of loop or arc positions and shield parameters, the loop and arc positions can be found to maximize a desired order of harmonic  $N$ . This, again, can be generalized to remove the set of undesired harmonic fields of order  $n \in \mathbb{Z} : n \in [n'_1, n'_N]$  and degree  $M$  through the set of simultaneous equations using pairs of symmetric and anti-symmetric loops or arcs at positions  $d_i$  and with axial turn ratios  $I_i^z$ . This is illustrated for zonal symmetric and anti-symmetric loops in Fig. 5b-c. The road map of this harmonic selection process is summarized in Fig. 6.

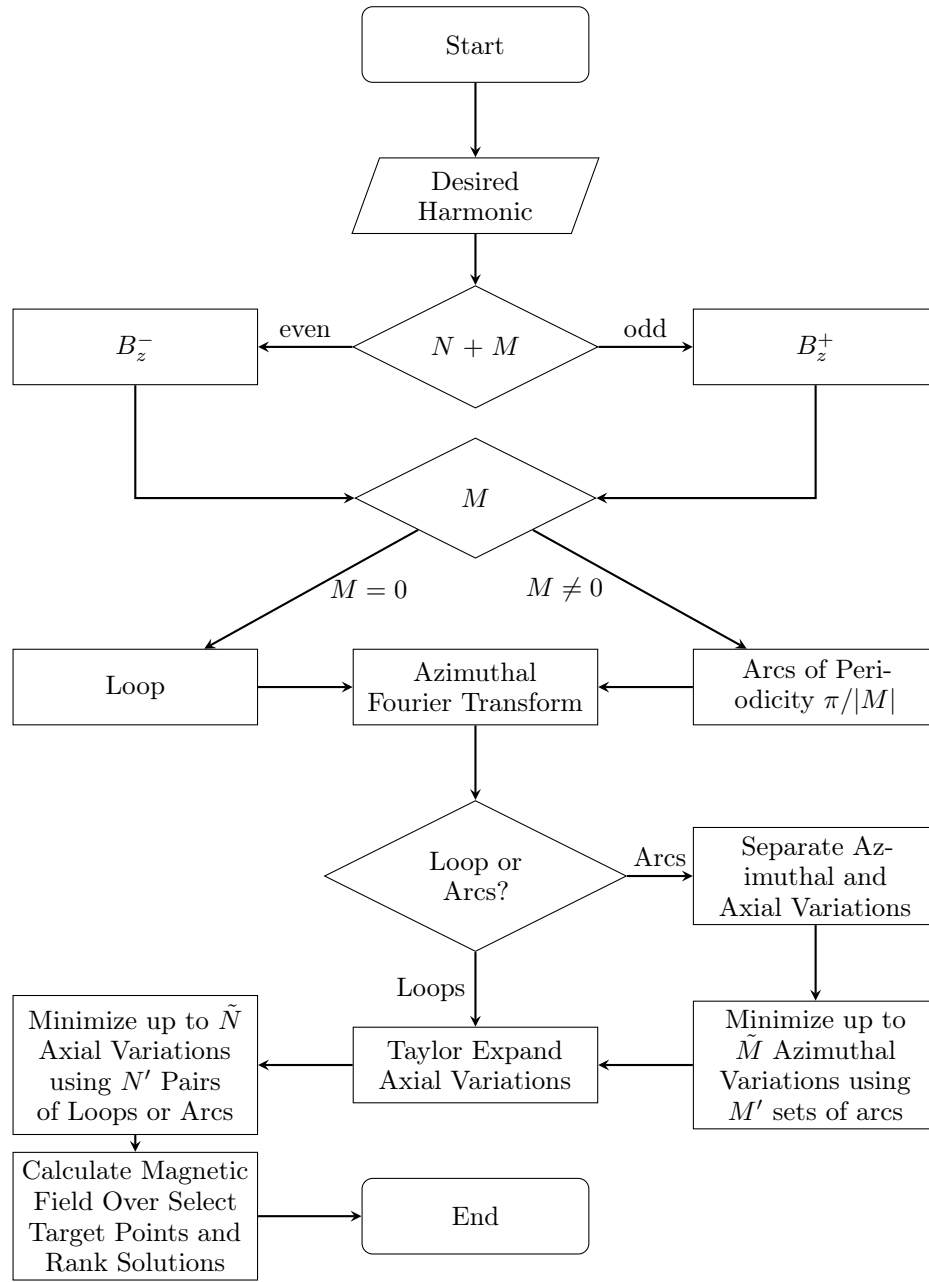


FIG. 6: Flow diagram describing the harmonic minimization method for generating a desired harmonic of order  $N$  and degree  $M$  using  $N'$  axial pairs of loops or arcs with  $M'$  arcs at each axial position.

**Example: Zonal linear gradient**

In this section, we apply the above analytical model to the case of an anti-Helmholtz pair within the bore of a cylindrical high-permeability cylinder (Fig. 7). The anti-Helmholtz configuration uses a pair of anti-symmetric axial loops to generate a scalar harmonic field,  $Z_2$ , which produces an axial linear gradient,  $dB_z/dz$ . The optimal loop position in free space,  $d = (\sqrt{3}/2)\rho_c$ , can be derived by eliminating the cubic variations in the generated field, i.e. the  $Z_4$  scalar harmonic<sup>1</sup>. In Fig. 8a and Fig. 8b we examine the field linearity of the anti-Helmholtz coils located, respectively, in free space and within a cylindrical magnetic shield of aspect ratio  $L_s/(2\rho_s) = 1$ . The presence of the magnetic shield affects the inductance of the coils and the profile of the field that they generate. In particular, coupling to the shield increases the inductance of the coils and the field gradient that they generate by approximately a factor of two. In addition, the magnetic shield amplifies the non-zero cubic variations in the field profile, causing it to deviate from a linear variation and reducing, by a factor of approximately three, the volume (bounded by dot-dashed curves in Fig. 8) wherein the generated and desired field gradient are within 1% of one another. Evidently, new optimal coil separations must be determined to improve the accuracy of the magnetic field that they generate in shielded environments.

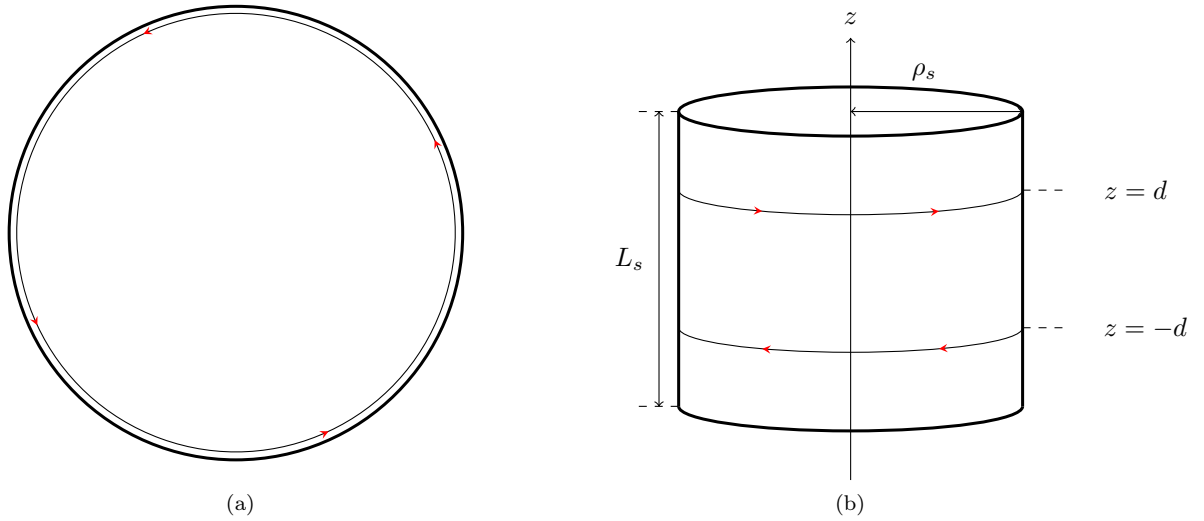


FIG. 7: Schematic diagram of an anti-symmetric pair of current-carrying loops of radius  $\rho_s$  showing (a) their azimuthal position (thin black circle with red arrow heads indicating current flow direction) within the magnetic shield (thick circle) and (b) their axial positions at  $z = \pm d$  placed symmetrically from the axial center at  $z = 0$  of a closed magnetic shield of radius  $\rho_s$  and length  $L_s = 2\rho_s$ .

The axial magnetic field generated by a pair of loops with counter-flowing currents and located co-axially on the interior surface of the high-permeability shield is, from (17), (20), and (21),

$$B_z(\rho, \phi, z) = \frac{2\mu_0 I}{L_s} b_0^-(\rho, z; d). \quad (29)$$

As explained in the previous section, any given magnetic profile in the system can be found by expanding the spatially-varying functions. By expanding these functions, we can group the spatial variations into their constituent spherical harmonic functions, and thereby determine how their effective magnitudes relate to the coil parameters. Using (23), and substituting the well-known series expansions,

$$I_m(x) = \sum_{l=0}^{\infty} \frac{1}{l!(l+m)!} \left(\frac{x}{2}\right)^{2l+m} \quad \text{and} \quad \sin(x) = \sum_{l=0}^{\infty} \frac{(-1)^l x^{2l+1}}{(2l+1)!}, \quad (30)$$

the axial field generated by the anti-symmetric pair (29) can be written in terms of the harmonic fields

$$B_z(\rho, \phi, z) = \frac{2\mu_0 I}{\pi} \left( z\tilde{C}_{2,0}(d, \rho_s, L_s) + \left(\frac{z\rho^2}{4} - \frac{z^3}{6}\right)\tilde{C}_{4,0}(d, \rho_s, L_s) + \dots \right), \quad (31)$$

where the effective harmonic magnitudes are given by

$$\tilde{C}_{2n,0}(d, \rho_s, L_s) = \frac{1}{L_s^{2n-1}} \sum_{p=1}^{\infty} (2p-1)^{2n-1} \frac{\sin\left(\frac{\pi d(2p-1)}{L_s}\right)}{I_0\left(\frac{\pi(2p-1)\rho_s}{L_s}\right)}. \quad (32)$$

Using (32) the optimal positions,  $z = \pm d$ , of the coils in an anti-symmetric pair can be determined so that the

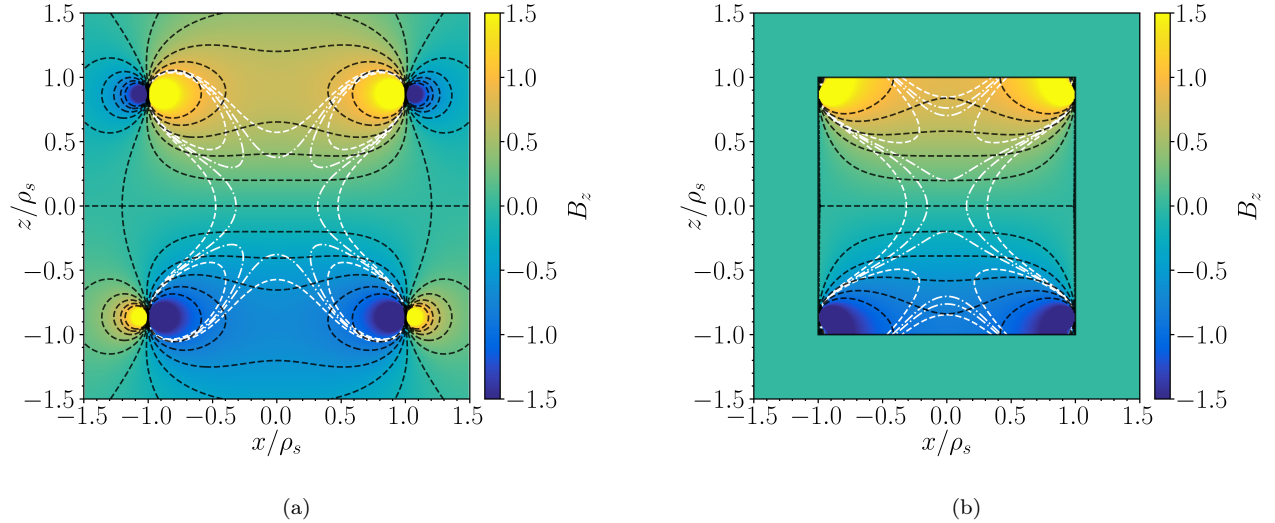


FIG. 8: Color maps showing the magnitude of the normalized axial magnetic field,  $B_z$ , in the  $xz$ -plane generated by the coil depicted in Fig. 7 in the anti-Helmholtz arrangement with separation,  $d = \pm(\sqrt{3}/2)\rho_s$  in two situations (a) in free space and (b) placed symmetrically around the origin of a closed magnetic shield of radius  $\rho_s$  and length  $L_s = 2\rho_s$  (solid black outline). White contours enclose the region where the field deviates from the target field by 5% (dashed curves) and 1% (dot-dashed curves). Black contours represent lines of constant magnetic flux (dashed curves). The resistance, field per unit current, and inductance of the coil both in free space and inside a unit length magnetic shield are presented in Table I.

leading-order error term from the desired field is removed when the coils are enclosed by a shield with a given aspect ratio.

$$\tilde{C}_{4,0}(d, \rho_s, L_s) = \frac{1}{L_s^3} \sum_{p=1}^{\infty} (2p-1)^3 \frac{\sin\left(\frac{\pi d(2p-1)}{L_s}\right)}{I_0\left(\frac{\pi(2p-1)\rho_s}{L_s}\right)} = 0. \quad (33)$$

In Fig. 9a, we show the optimal separation calculated versus the shield aspect ratio by an exhaustive numerical search. Figure 9b shows the corresponding variation of the gradient per unit current. The red dotted lines in Fig. 9a and Fig. 9b show, respectively, the optimal separation,  $d = 0.824\rho_s$ , in the limit that the shield aspect ratio tends to infinity, and its corresponding gradient per unit current, 1.23. The blue dotted lines in Fig. 9a and Fig. 9b are, respectively, the coil separation for the standard anti-Helmholtz configuration,  $d = \sqrt{3}\rho_s/2$  and its gradient per unit current, 0.806, that is generated in free space. Due to the interaction and finite length of the magnetic shield there exists a shield aspect ratio,  $0 < L_s/(2\rho_s) \lesssim 0.831$ , where no coil separation entirely removes the cubic variation in the field. In this case, to determine the optimal separation, contributions from both the cubic and quintic variations should be minimized, but not nulled entirely, to achieve the most uniform field linearity for a given application.

We can generalize the above example to the case of  $N'$  loops at positions,  $d_i$ , which are chosen to minimize  $\tilde{N}$  harmonics

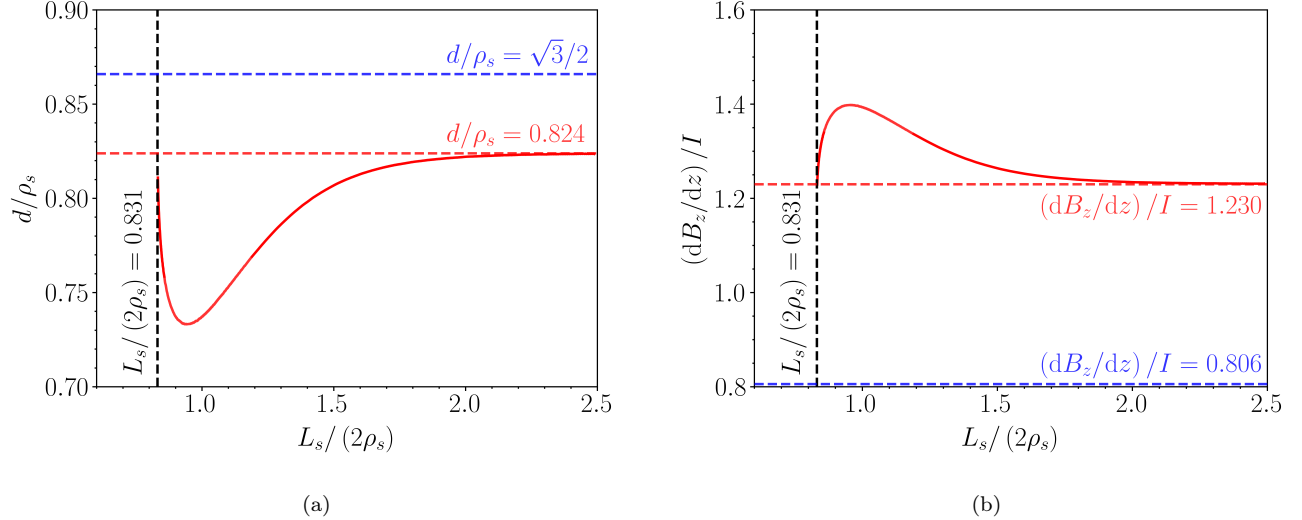


FIG. 9: (a) Optimal normalized separation,  $d/\rho_s$ , of the anti-symmetric pair, depicted in Fig. 7, to generate the zonal  $Z_2$  harmonic as the length of the shield increases (red curve). Horizontal dashed lines (red and blue) show the analytical values of  $d = 0.824\rho_s$  and  $d = (\sqrt{3}/2)\rho_s$  obtained in the long shield limit ( $L_s \gg 2\rho_s$ ) and in free space, respectively. (b) Gradient per current,  $(dB_z/dz)/I$ , of the optimal anti-symmetric pair as the length of the shield increases (red curve). Horizontal dashed lines (red and blue) show the values of  $dB_z/dz = 1.230I$  and  $dB_z/dz = 0.806I$  obtained in the long shield limit and in free space, respectively. Vertical dashed line (black) in (a) and (b) shows the minimum shield length  $L_s = 1.62\rho_s$  below which no optimal solution can be found.

by using (32) to generate the set of simultaneous equations

$$\min_{I_i^z, d_i} \left( \sum_{i=1}^{N'} \frac{I_i^z}{L_s^{2n-1}} \sum_{p=1}^{\infty} (2p-1)^{2n-1} \frac{\sin\left(\frac{\pi d_i (2p-1)}{L_s}\right)}{I_0 \left(\frac{\pi (2p-1) \rho_s}{L_s}\right)} \right), \quad n \in \mathbb{Z} : n \in [2, \tilde{N} + 1]. \quad (34)$$

The manual removal of multiple harmonic fields is difficult and time consuming because each undesired harmonic must be analyzed in turn in order to find the optimal coil separations. But, as  $n$  increases, the magnitude of each harmonic becomes increasingly sensitive to the precise values of  $d_i$ . Consequently, the domain in which a solution exists that eliminates many harmonics becomes progressively more challenging to find. Moreover, to manufacture these nested designs easily, the axial turn ratios  $I_i^z$  should be integers within an order of magnitude range of one another, which further increases the difficulty in finding solutions.

Clearly, unlike the simultaneous equations used to determine optimal angular lengths, the construction of this problem is nontrivial, and requires a level of intuition to solve effectively. The parity of each undesired harmonic magnitude over the domain of allowed  $d_i$  can be determined and combined to find a suitable range of  $I_i^z$  where solutions exist. From this, the domain where  $d_i$  values exist that solve the problem can be searched efficiently. The process for determining the search regions could be automated and be performed whenever a different harmonic field is selected or the aspect ratio of the shield is altered. However, this is time consuming and cannot be generalized effectively. This bounded multi-dimensional minimization problem with integer constraints is an ideal candidate for a multi-objective optimization procedure that allows optimal positions and turn ratios to be found in a computationally-efficient manner.

## V. GENETIC ALGORITHM OPTIMIZATION

There is a vast array of optimization methods that can be used to find optimal solutions to minimization problems. The applicability of these methods depends on the functional form and number of different of objective functions. Multi-objective optimization describes a group of methods that allow the simultaneous optimization of many functions. These methods enable the optimization of conflicting objectives, resulting in a higher-quality solution. Here, we use a genetic algorithm to solve the non-linear, mixed-integer, multi-objective optimization problem. The optimal continuous

separations,  $d_i$ , and discrete turn ratios,  $I_i^z$ , for  $N'$  loops or arcs are found by minimizing the amplitudes of a set of undesired harmonic fields. These amplitudes are the objective functions, constrained by the minimum distance,  $D$ , between any two loops and the maximum turn ratio,  $I_{\max}^z$ . We formulate the optimization problem by using the set of arbitrary user-defined undesired harmonic fields of order  $n \in \mathbb{Z} : n \in [\tilde{n}_1, \tilde{n}_{\tilde{N}}]$  and degree  $M$  as the objective functions:

$$\begin{cases} \min f_1 = \tilde{C}_{\tilde{n}_1, M}(\rho_s, L_s; d_1, \dots, d_{N'}, I_1, \dots, I_{N'}), \\ \vdots \\ \min f_{\tilde{N}} = \tilde{C}_{\tilde{n}_{\tilde{N}}, M}(\rho_s, L_s; d_1, \dots, d_{N'}, I_1, \dots, I_{N'}). \end{cases} \quad (35)$$

Here, we assume that the required azimuthal variations have been eliminated using (25) and that the remaining undesired harmonics constitute the  $\tilde{N}$  leading-order error terms of degree  $M$  that exist within axial magnetic field. The search domain of the design parameters are

$$\begin{cases} D/2 < d_1 < d_2 - D, \\ d_1 + D < d_2 < d_3 - D, \\ \vdots \\ D + d_{N'-1} < d_{N'} < L_s/2, \\ 1 \leq I_1^z \leq I_{\max}^z, \\ -I_{\max}^z \leq I_2^z \leq I_{\max}^z, \\ \vdots \\ -I_{\max}^z \leq I_{N'}^z \leq I_{\max}^z, \end{cases} \quad (36)$$

where the physical constraints on the system are that the axial turn ratios are less than the maximum axial turn ratio  $I_{\max}^z$ , the separation of any two nested loops or arcs is less than the minimum separation  $D$ , and the outer loop arc is axially inside the shield  $d_{N'} < L_s/2$ .

To solve the problem, we use the MATLAB function `gamultiobj()`, from the multi-objective genetic algorithm toolbox, which implements the NSGA-II algorithm<sup>41</sup>. We modify the mutation, crossover, and creation functions to allow integer turn ratios and continuous value separations to be optimized simultaneously. To find solutions effectively, the population size, number of generations, and function tolerance are changed to reflect the number of design parameters and objective functions required for a specific design.

We now present two examples of optimized coil designs found through the use of the genetic algorithm. Firstly, we design an improved linear gradient field,  $Z_2$ , and compare this result to the previous anti-Helmholtz design. Then, we design a transverse bias field,  $T_{1,1}$ , where  $m = n = 1$ , which, importantly, is absent from the axial field in (12). We demonstrate how the desired field can be indirectly selected by removing the leading-order error terms that are present in the axial field. This optimized transverse coil is then compared to an equivalent non-optimized transverse coil.

### Example I: Improved linear gradient field

To find an improved linear gradient field we choose to search for solutions using a four-pair anti-symmetric loop setup within a high-permeability magnetic shield of aspect ratio  $L_s/(2\rho_s) = 1$ . The axial magnetic field is given by

$$B_z(\rho, \phi, z) = \frac{2\mu_0}{L_s} \sum_{i=1}^4 I_i^z b_0^-(\rho, z; d_i), \quad (37)$$

and we choose to minimize the first three leading-order error terms

$$\begin{cases} \min f_1 = \tilde{C}_{4,0}(\rho_s, L_s; d_1, \dots, d_4, I_1^z, \dots, I_4^z), \\ \min f_2 = \tilde{C}_{6,0}(\rho_s, L_s; d_1, \dots, d_4, I_1^z, \dots, I_4^z), \\ \min f_3 = \tilde{C}_{8,0}(\rho_s, L_s; d_1, \dots, d_4, I_1^z, \dots, I_4^z), \end{cases} \quad (38)$$

which, from (32), are given by

$$\tilde{C}_{2n,0} = \sum_{i=1}^4 \frac{I_i^z}{L_s^{2n-1}} \sum_{p=1}^{\infty} (2p-1)^{2n-1} \frac{\sin\left(\frac{\pi d_i(2p-1)}{L_s}\right)}{I_0\left(\frac{\pi(2p-1)\rho_s}{L_s}\right)}. \quad (39)$$

We constrain the separation of the wires such that  $D = 0.01\rho_s$ , towards the upper bound of the small wire diameter approximation, limit the maximum turn ratio to  $I_{\max}^z = 9$ , and search for optimal values of  $[d_1, \dots, d_4]$  and  $[I_1^z, \dots, I_4^z]$ . The genetic algorithm outputs numerous Pareto-optimal solutions where the first three undesired contributions are minimized, meaning that many solutions exist where no undesired harmonic can be further minimized without increasing the magnitude of another undesired harmonic. To filter these solutions, we rank them according to their stability by adjusting the wire placements slightly and analyzing their performance. The most stable coil configuration, which almost entirely eliminates the first three unwanted harmonics from the system, is shown in Fig. 10. The color maps in Fig. 11 show the magnitude of the axial magnetic field component,  $B_z$ , generated (a) in free space and (b) inside the high-permeability magnetic shield. Due to the improved linearity of the magnetic field profile that results from the additional coil pairs, the volume of the region within which the field achieved is within 1% of the desired field (i.e. within the dot-dashed curves) is seven times larger than that produced by standard anti-Helmholtz coils inside the same magnetic shield (see Fig. 8). This demonstrates the effectiveness of our design methodology and the applicability of the genetic algorithm optimization to this problem. The resistance and inductance of the improved multi-pair system and shield are, however, an order of magnitude larger than for the standard anti-Helmholtz configuration. The resistance, magnetic field gradient per unit current, and inductance for various coil configurations in both free space and inside a magnetic shield of unit length are summarized in Table. I.

Although not guaranteed, there could exist other multi-pair coil designs that minimize more undesired harmonics than the example shown in Fig. 10. However, the effect of removing high-order harmonics eventually reaches a point of diminishing returns where the sensitivity of the harmonic magnitudes to the precise position of the wire loops or arcs is so large that a practical solution can not be obtained. The unique benefits of discrete coil optimization are lost if too many harmonics need to be nulled and the design becomes more complex, meaning that coarse discretization of an optimized continuum current distribution on the surface of a cylinder could yield better results<sup>32</sup>.

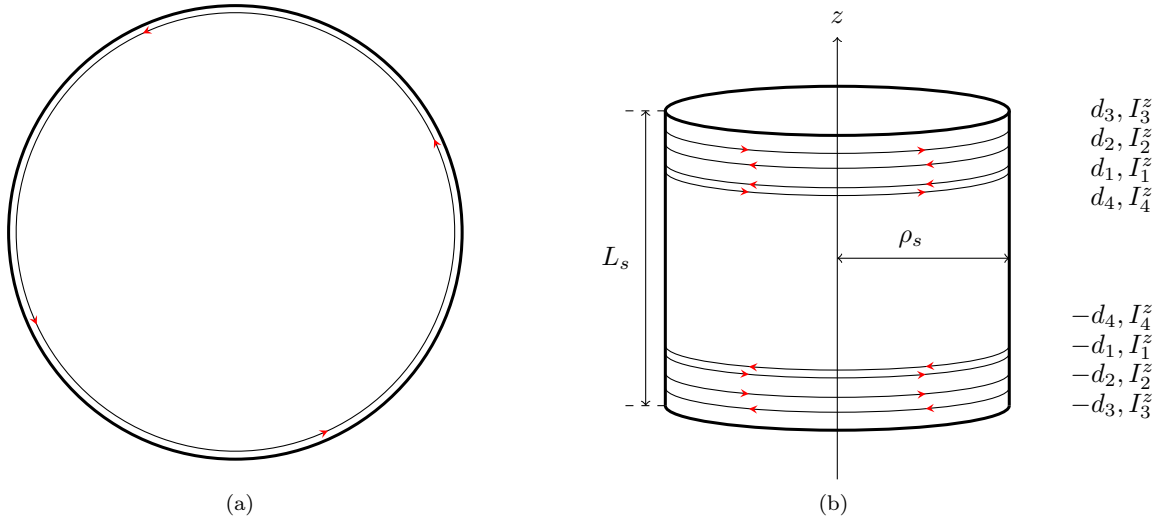


FIG. 10: Schematic diagram of four anti-symmetric loop pairs of radius  $\rho_s$  showing the (a) azimuthal variations and (b) axial positions  $z = \pm d_i$ , where  $d_i = [0.592, 0.645, 0.777, 0.878]\rho_s$ , with axial turn ratios  $I_i^z = [3, -3, -2, 3]$ , for  $i \in \mathbb{Z} : i \in [1, 4]$ , placed symmetrically around the origin of a closed magnetic shield of radius  $\rho_s$  and length  $L_s = 2\rho_s$ .

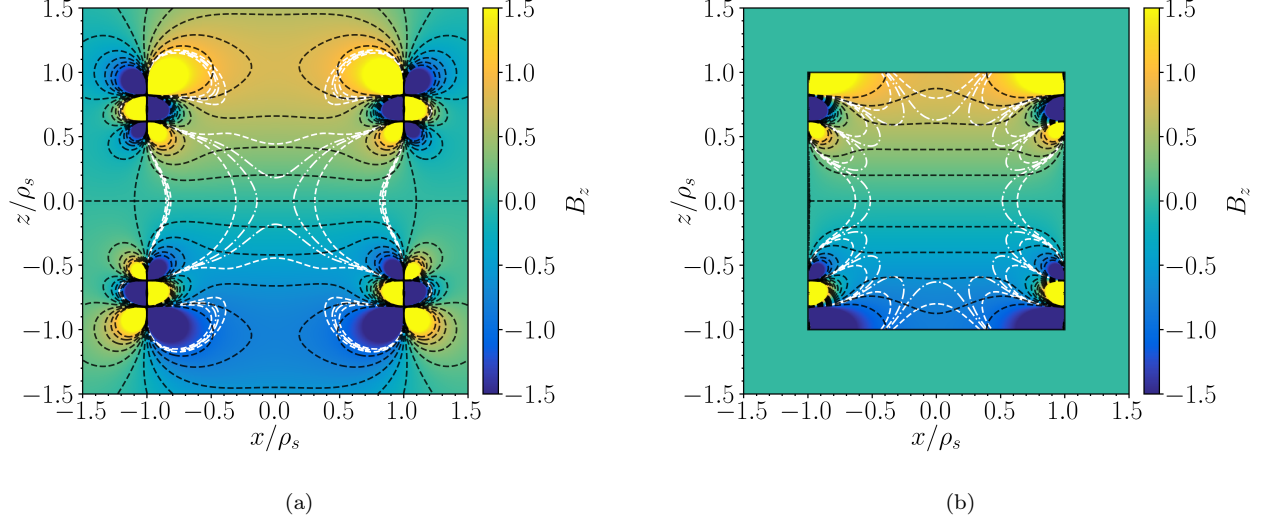


FIG. 11: Color maps showing the magnitude of the normalized axial magnetic field,  $B_z$ , in the  $xz$ -plane generated the design depicted in Fig. 10 in two situations (a) in free space and (b) placed symmetrically around the origin of a closed magnetic shield of radius  $\rho_s$  and length  $L_s = 2\rho_s$  (solid black outline). White contours enclose the region where the field deviates from the target field by 5% (dashed curves) and 1% (dot-dashed curves). Black contours represent lines of constant magnetic flux (dashed curves). The resistance, gradient per unit current, and inductance of the coil both in free space and inside a unit length magnetic shield are presented in Table I.

### Example II: transverse bias field

A transverse bias field,  $B_x$ , can be represented by a single spherical harmonic field of order  $n = 1$  and degree  $m = 1$ . Consequently, the symmetries within the desired harmonic field correspond to the anti-symmetric tesseral coil basis, with azimuthal periodicity  $\pi$ , as shown in Fig. 4d and Fig. 3b, respectively. As mentioned above, the harmonic  $T_{1,1}$  is not present within the axial field. However, we can still search for optimized transverse coils using the axial magnetic field. Here, we use setup comprising four pairs of coils with three overlapping arcs of different angular lengths, which generate an axial magnetic field

$$B_z(\rho, \phi, z) = \frac{4\mu_0}{L_s} \sum_{m=1}^{\infty} \sum_{i=1}^4 \sum_{j=1}^3 I_i^\varphi I_j^\varphi b_m^-(\rho, z; d_i) \Phi_j^m \cos(m\phi), \quad (40)$$

where

$$\Phi^m(\varphi_j) = \frac{\sin(m\varphi_j)}{\pi m} (1 - (-1)^m). \quad (41)$$

Using three angular lengths, we are able to remove the first three sets of harmonics of degrees  $m = (3, 5, 7)$  by solving the set of simultaneous equations

$$\min_{\varphi_j} \left( \sum_{j=1}^{M'} I_j^\varphi \sin((2\nu + 1)\varphi_j) \right), \quad \nu \in \mathbb{Z} : \nu \in [1, 3]. \quad (42)$$

For simplicity and ease of manufacturing, we choose  $I_j^\varphi = [1, 1, 1]$ , and find optimized angular lengths of  $\varphi_j = [1.367, 1.101, 0.592]$ . Having removed the leading-order azimuthal errors of degrees  $m = (3, 5, 7)$ , the first three

leading-order error terms in the desired field affect the axial field component (40), and are given by

$$\tilde{C}_{2n-1,1} = \sum_{i=1}^N I_i^z \sum_{p=1}^{\infty} (2p-1)^{2n} \frac{\sin\left(\frac{\pi d_i(2p-1)}{L_s}\right)}{I_1\left(\frac{\pi(2p-1)\rho_s}{L_s}\right)}, \quad n \in \mathbb{Z} : n \in [2, 4], \quad (43)$$

where the objective functions are written as

$$\begin{cases} \min f_1 = \tilde{C}_{3,1}(\rho_s, L_s; d_1, \dots, d_4, I_1, \dots, I_4), \\ \min f_2 = \tilde{C}_{5,1}(\rho_s, L_s; d_1, \dots, d_4, I_1, \dots, I_4), \\ \min f_3 = \tilde{C}_{7,1}(\rho_s, L_s; d_1, \dots, d_4, I_1, \dots, I_4). \end{cases} \quad (44)$$

Again, we impose the constraint,  $D = 0.01\rho_s$ , on the separation between adjacent wires and limit the maximum turn ratio such that  $I_{\max}^z = 9$ . As in example I, we select the most stable Pareto-optimal solution, which effectively eliminates the first two leading-order error terms and greatly reduces the third. The solution is shown graphically in Fig. 12, where the transverse field variations in the  $xz$ -plane in free space and inside the magnetic shield are shown in Fig. 13a-b, respectively. Since no standard transverse field design exists that fits within a magnetic shield with the specified aspect ratio, we use the non-optimized saddle coil shown in Fig. 14, with separation  $d = L_s - \rho_w$  and the same azimuthal variation shown in Fig. 12a, for comparison with our optimized design. The transverse field variations in the  $xz$ -plane in free space and inside the magnetic shield generated by the non-optimized coil are shown in Fig. 15a-b. The optimized transverse coil generates a field that is homogeneous to within 1% variation throughout a volume that is approximately four times greater than the non-optimized design. However, the resistance and inductance for the optimized transverse field coils are, respectively, three and ten times larger than the non-optimized arrangement. The field per unit current is also a factor of seven lower in the optimized system compared with the non-optimized coils. The resistance, field per unit current, and inductance, for both optimized and non-optimized designs in both free space and within the magnetic shield are summarized in Table. I.

Additional constraints could be added to the optimization to minimize the resistance, inductance, or to maximize the field per current. However, this would come at a cost of field fidelity. For a given experimental situation, the Pareto-optimal solutions should be ranked according to the performance that they give against specified operating parameters.

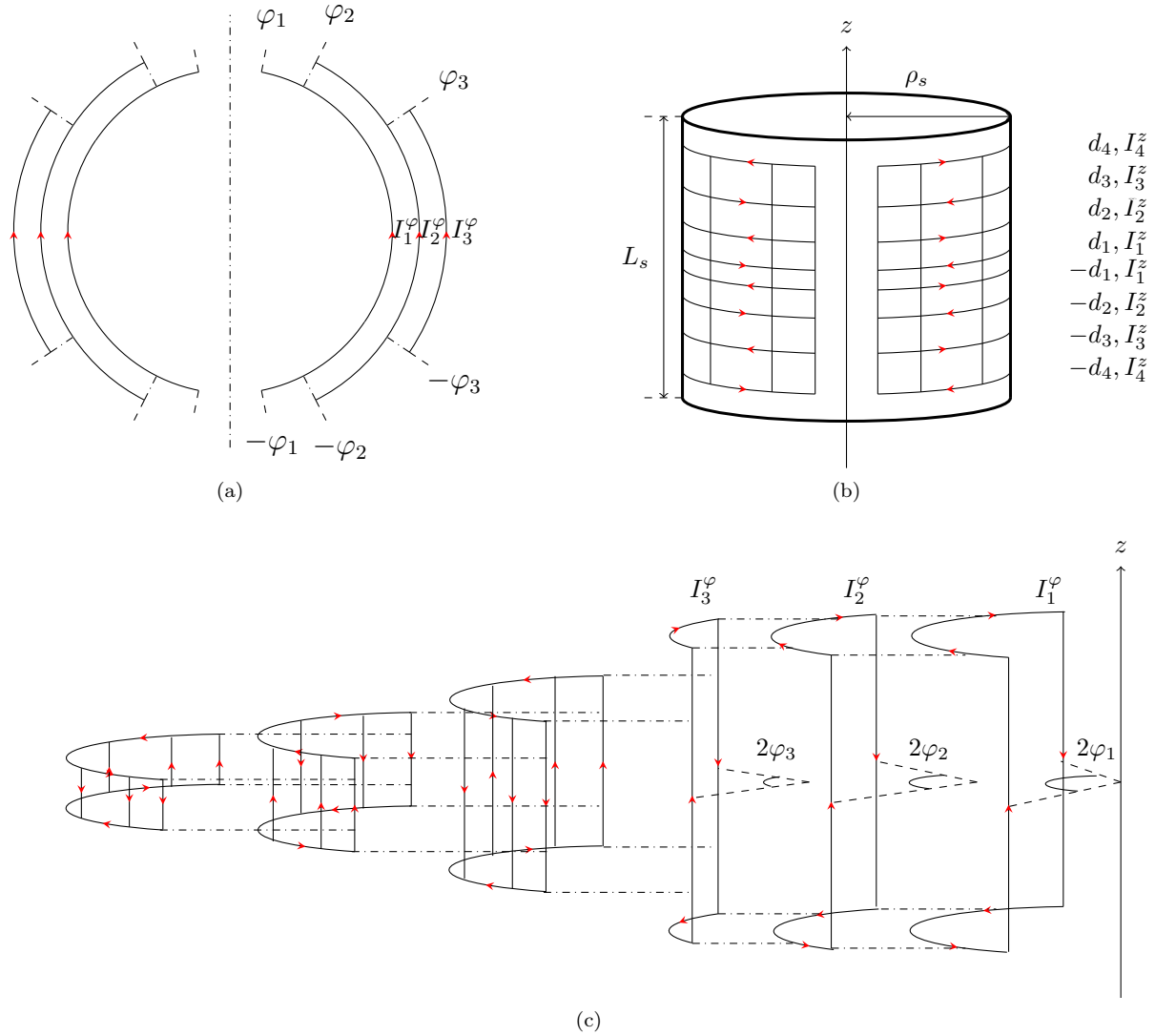


FIG. 12: Schematic diagram of four axial anti-symmetric arc pairs of radius  $\rho_s$  with three azimuthal variations for each pair, showing the (a) azimuthal variations of periodicity,  $\pi$ , for the three separate angular lengths  $\varphi_j = [1.376, 1.101, 0.593]$  with azimuthal turn ratios  $I_j^\varphi = [1, 1, 1]$ , for  $j \in \mathbb{Z} : j \in [1, 3]$ , and (b) axial positions  $z = \pm d_i$ , where  $d_i = [0.068, 0.226, 0.525, 0.810]\rho_s$ , with axial turn ratios  $I_i^z = [5, -3, 2, -1]$ , for  $i \in \mathbb{Z} : i \in [1, 4]$ , placed symmetrically around the origin of a closed magnetic shield of radius  $\rho_s$  and length  $L_s = 2\rho_s$ . (c) Shows an expanded schematic diagram of one azimuthal section of the coil depicted in (a)-(b) for clarity.

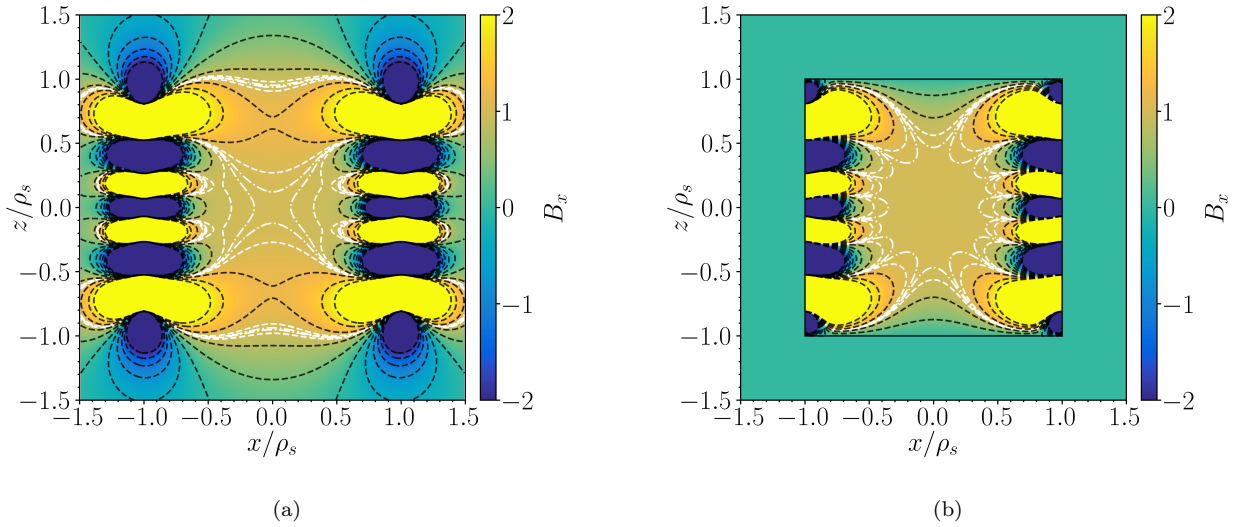


FIG. 13: Color maps showing the magnitude of the normalized transverse magnetic field,  $B_x$ , in the  $xz$ -plane generated the design depicted in Fig. 12 in two situations (a) in free space and (b) placed symmetrically around the origin of a closed magnetic shield of radius  $\rho_s$  and length  $L_s = 2\rho_s$  (solid black outline). White contours enclose the region where the field deviates from the target field by 5% (dashed curves) and 1% (dot-dashed curves). Black contours represent lines of constant magnetic flux (dashed curves). The resistance, field per unit current, and inductance of the coil both in free space and inside a unit length magnetic shield are presented in Table I.

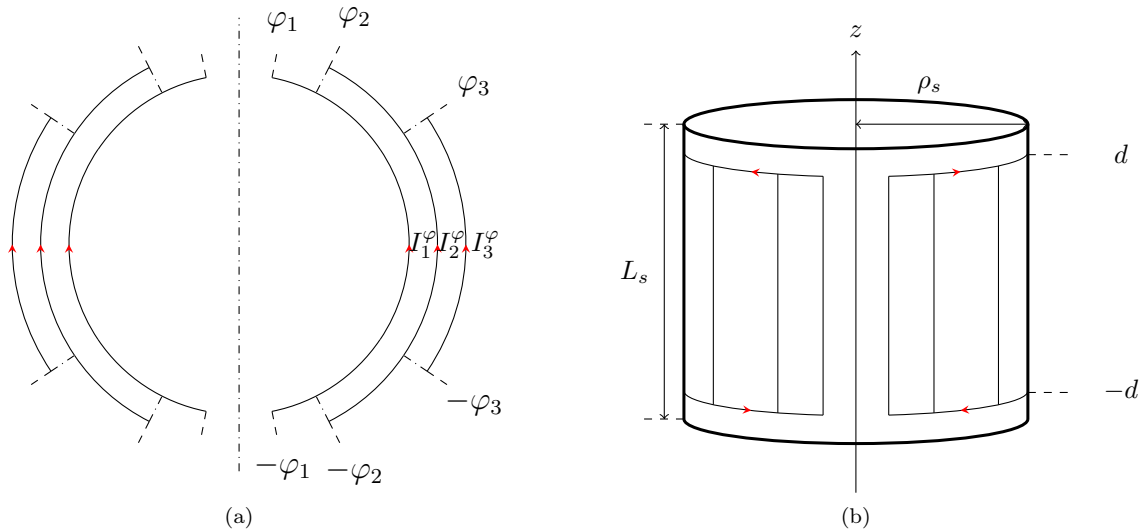


FIG. 14: Schematic diagram of one axial anti-symmetric arc pair of radius  $\rho_s$  with three azimuthal variations, showing the (a) azimuthal variations of periodicity,  $\pi$ , for the three separate angular lengths  $\varphi_j = [1.376, 1.101, 0.593]$  with azimuthal turn ratios  $I_j^\varphi = [1, 1, 1]$ , for  $j \in \mathbb{Z} : j \in [1, 3]$ , and (b) axial positions  $z = \pm d$ , where  $d = (L_s/2 - \rho_w)\rho_s$ , placed symmetrically around the origin of a closed magnetic shield of radius  $\rho_s$  and length  $L_s = 2\rho_s$ .

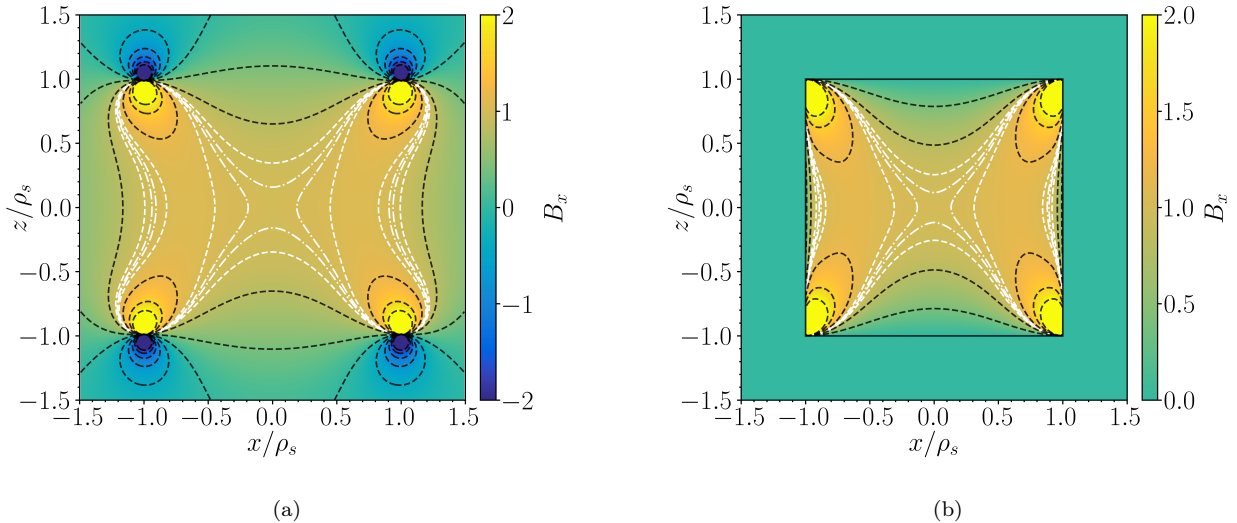


FIG. 15: Color maps showing the magnitude of the normalized transverse magnetic field,  $B_x$ , in the  $xz$ -plane generated by the design depicted in Fig. 14 in two situations (a) in free space and (b) placed symmetrically around the origin of a closed magnetic shield of radius  $\rho_s$  and length  $L_s = 2\rho_s$  (solid black outline). White contours enclose the region where the field deviates from the target field by 5% (dashed curves) and 1% (dot-dashed curves). Black contours represent lines of constant magnetic flux (dashed curves). The resistance, field per unit current, and inductance of the coil both in free space and inside a unit length magnetic shield are presented in Table I.

Coil Design		Resistance ( $\Omega$ )	Field / Current ( $\mu\text{T}/\text{Am}^{N-1}$ )	Inductance ( $\mu\text{H}$ )
Anti-Helmholtz	Unshielded	0.134	3.28	6.19
	Shielded		7.16	12.4
Improved Linear Gradient	Unshielded	1.48	2.74	131
	Shielded		6.92	184
Non-Optimized Transverse	Unshielded	1.03	4.21	51.8
	Shielded		6.88	104
Optimized Transverse	Unshielded	3.63	0.65	724
	Shielded		1.04	1010

TABLE I: The resistance  $R$ , field per unit current  $C_{NM}/I$ , and inductance  $L$ , for the example coils with wire radius  $\rho_w = 0.5$  mm, described in the text and located both in free space and inside an magnetic shield of unit length,  $L_s = 1$  m, and radius  $\rho_s = 0.5$  m. The anti-Helmholtz and improved linear gradient coils are shown in Fig. 7 and Fig. 10, respectively, and generate an  $N = 2$  zonal harmonic field,  $Z_2$ . The non-optimized and optimized transverse coils are shown in Fig. 14 and Fig. 12, respectively, and generate an  $N = 1$ ,  $M = 1$  tesseral harmonic field,  $T_{1,1}$ .

## VI. CONCLUSION

In summary, we have introduced a coil design method based around simple discrete current-carrying loops and arcs whose geometry can be optimized accurately to generate any physically-attainable magnetic field within a high-permeability cylindrical magnetic shield. To do this, we used a Green's function that satisfies the boundary conditions at the surface of the high-permeability cylinder and determined field expansions that enable elimination of deviations from the desired field to specified expansion order when the coil is on the magnetic shield's surface. We

then presented a discrete coil expansion basis composed of unit-coil building blocks and decomposed the magnetic field that they generate into spherical harmonic terms in free space. Next, for specific designs, we related the coil parameters, namely the wire spacing, angular arc lengths, and the currents through pairs of loops and arcs, to a set of harmonic fields chosen to reflect the form of the desired field profiles. Finally, we used this decomposition to find optimal discrete coil designs using a genetic algorithm optimization procedure.

Using the anti-Helmholtz pair as an example, we found that the central volume within which the field gradient varies by less than 1% diminished by a factor of three when the coils were moved from free space to within the bore of a high-permeability cylindrical shield. We used our model to determine the optimal separation of an anti-Helmholtz pair in a magnetic shield of arbitrary length and thereby restore the uniformity of the magnetic field gradient. Taking this optimization one step further, we formulated simultaneous equations to remove multiple harmonic fields using multiple current loops and arcs and used a genetic algorithm to find optimized turn ratios and wire separations. We used this optimization procedure to design high-fidelity transverse bias and linear-gradient fields. In particular, we found that this optimization process increased the volume within which variations of the field gradient are less than 1% by a factor of seven compared to the standard anti-Helmholtz arrangement in the same shield. However, this improved field fidelity increases the power consumption and system inductance.

The analytical model, discrete coil basis, and optimization procedure presented here allow the efficient design of compact discrete coils that generate accurate user-specified desired magnetic fields within a finite length cylindrical magnetic shield. This methodology will facilitate new miniaturized technologies that require custom magnetic fields within a magnetically shielded environment. The performance of existing magnetic field-generating systems can be improved by retrofitting discrete coil systems that are optimized by our methodology. Additional objective functions could be added to the method such as the sensitivity of the harmonic field magnitudes to wire placement or the minimization of power consumption or inductance. These additions may reduce field fidelity but would allow the method to be tailored to the needs of individual experiments and installations. Further research could investigate the use of discrete planar coils on the surface of the end-plates to enable more power-efficient and accurate designs.

## ACKNOWLEDGMENTS

We acknowledge support from the UK Quantum Technology Hub in Sensors and Timing, funded by the UK Engineering and Physical Sciences Research Council (EP/M013294/1) and from Innovate UK Project 44430 MAG-V: Enabling Volume Quantum Magnetometer Applications through Component Optimisation & System Miniaturisation. The authors M.P., P.J.H., T.M.F., M.J.B., and R.B. declare that they have a patent pending to the UK Government Intellectual Property Office (Application No.1913549.0) regarding the magnetic field optimization techniques described in this work. N.H, M.J.B, and R.B also declare financial interests in a University of Nottingham spin-out company, Cerca. The authors have no other competing financial interests.

## DATA AVAILABILITY STATEMENT

The data that support the findings of this study are available from the corresponding author upon reasonable request.

## APPENDIX A: AXIAL DIFFERENTIATION OF SPHERICAL HARMONICS

Let us consider the harmonic

$$R_{n,m}(r, \theta, \phi) = r^n P_{n,|m|}(\cos \theta) \begin{cases} \cos(|m|\phi) & m \geq 0 \\ \sin(|m|\phi) & m < 0 \end{cases}. \quad (45)$$

The differential of an arbitrary curvilinear coordinate system with respect to another may be expressed as

$$\frac{\partial R_{n,m}(r, \theta, \phi)}{\partial \chi_i} = \sum_j \frac{\partial \xi_j}{\partial \chi_i} \frac{\partial}{\partial \xi_j} R_{n,m}(r, \theta, \phi). \quad (46)$$

Using this, the differential in cylindrical coordinates may be determined. Spherical polar coordinates can be written as

$$r = \sqrt{\rho^2 + z^2}, \quad \theta = \cos^{-1} \left( \frac{z}{\sqrt{\rho^2 + z^2}} \right), \quad \phi = \phi. \quad (47)$$

As a result, the axial derivative is given by

$$\frac{\partial R_{n,m}(r, \theta, \phi)}{\partial z} = \left( \frac{\partial r}{\partial z} \frac{\partial}{\partial r} + \frac{\partial \theta}{\partial z} \frac{\partial}{\partial \theta} \right) R_{n,m}(r, \theta, \phi), \quad (48)$$

Using (46) and (47), the differential with respect to  $z$  is given simply by

$$\frac{\partial R_{n,m}(r, \theta, \phi)}{\partial z} = \left( \cos \theta \frac{\partial}{\partial r} - \frac{\sin \theta}{r} \frac{\partial}{\partial \theta} \right) R_{n,m}(r, \theta, \phi), \quad (49)$$

which, using (45), becomes

$$\frac{\partial R_{n,m}(r, \theta, \phi)}{\partial z} = r^{n-1} \begin{pmatrix} n \cos \theta P_{n,|m|}(\cos \theta) - \sin \theta \frac{\partial P_{n,|m|}(\cos \theta)}{\partial \theta} \\ \cos(|m|\phi) \\ \sin(|m|\phi) \end{pmatrix}. \quad \begin{matrix} m \geq 0 \\ m < 0 \end{matrix} \quad (50)$$

Directly substituting the relation from<sup>51</sup>

$$\frac{\partial P_{n,|m|}(\cos \theta)}{\partial \theta} = n \cot \theta P_{n,|m|}(\cos \theta) - \frac{n + |m|}{\sin \theta} P_{n-1,|m|}(\cos \theta) \quad (51)$$

into (50) yields the final expression

$$\frac{\partial R_{n,m}(r, \theta, \phi)}{\partial z} = (n + |m|) P_{n-1,|m|}(\cos \theta) \begin{pmatrix} \cos(|m|\phi) \\ \sin(|m|\phi) \end{pmatrix}. \quad \begin{matrix} m \geq 0 \\ m < 0 \end{matrix} \quad (52)$$

- <sup>1</sup>F. Roméo and D. I. Hoult, Magnet field profiling: analysis and correcting coil design, *Magn. Reson. Med.* **1**, 1 (1984).  
<sup>2</sup>S. Pissanetzky, Minimum energy MRI gradient coils of general geometry, *Meas. Sci. Technol.* **3**, 7 (1992).  
<sup>3</sup>M. Poole and R. Bowtell, Novel gradient coils designed using a boundary element method, *Concept Magn. Reson. B* **3**, 162–175 (2007).  
<sup>4</sup>N. Holmes, T. M. Tierney, J. Leggett, E. Boto, S. Mellor, G. Roberts, R.M. Hill, V. Shah, G.R. Barnes, M.J. Brookes, and R. Bowtell, Balanced, bi-planar magnetic field and field gradient coils for field compensation in wearable magnetoencephalography, *Sci. Rep.* **9**, 14196 (2019).  
<sup>5</sup>L.K. Forbes and S. Crozier, A novel target-field method for finite-length magnetic resonance shim coils: I. Zonal shims, *J. Phys. D: Appl. Phys.* **34**, 3447 (2001).  
<sup>6</sup>L.K. Forbes and S. Crozier, A novel target-field method for finite-length magnetic resonance shim coils: II. Tesseral shims, *J. Phys. D: Appl. Phys.* **35**, 839 (2002).  
<sup>7</sup>L.K. Forbes and S. Crozier, A novel target-field method for magnetic resonance shim coils: III. Shielded zonal and tesseral coils, *J. Phys. D: Appl. Phys.* **36**, 68 (2002).  
<sup>8</sup>X. Wu, Z. Pagel, B. S. Malek, T. H. Nguyen, F. Zi, D. S. Scheirer, and H. Müller, Gravity surveys using a mobile atom interferometer, *Sci. Adv.* **5**, 9 (2019).  
<sup>9</sup>V. Menoret, P. Vermeulen, N. L. Moigne, S. Bonvalot, P. Bouyer, A. Landragin, and B. Desruelle, Gravity measurements below  $10^{-9} g$  with a transportable absolute quantum gravimeter, *Sci. Rep.* **8**, 1 (2018).  
<sup>10</sup>M. J. Snadden, J. M. McGuirk, P. Bouyer, K. G. Haritos, and M. A. Kasevich, Measurement of the Earth's gravity gradient with an atom interferometer-based gravity gradiometer, *Phys. Rev. Lett.* **81**, 971 (1998).  
<sup>11</sup>K. Bongs, M. Holynski, J. Vovrosh, P. Bouyer, G. Condon, E. Rasel, C. Schubert, W. P. Schleich, and A. Roura, Taking atom interferometric quantum sensors from the laboratory to real-world applications, *Nat. Rev. Phys.* **1**, 731 (2019).  
<sup>12</sup>I. Moric, P. Laurent, P. Chatard, C.-M. de Graeve, S. Thomin, V. Christophe, and O. Grosjean, Magnetic shielding of the cold atom space clock PHARAO, *Acta Astronaut.* **102**, 287 (2014).  
<sup>13</sup>L. Liu, D.-S. Lü, W.-B. Chen, T. Li, Q.-Z. Qu, B. Wang, L. Li, W. Ren, Z.-R. Dong, J.-B. Zhao, W.-B. Xia, X. Zhao, J.-W. Ji, M.-F. Ye, Y.-G. Sun, Y.-Y. Yao, D. Song, Z.-G. Liang, S.-J. Hu, and Y.-Z. Wang, In-orbit operation of an atomic clock based on laser-cooled  $^{87}\text{Rb}$  atoms, *Nat. Commun.* **9**, 2760 (2018).  
<sup>14</sup>B. Patton, E. Zhivun, D. C. Hovde, and D. Budker, All-optical vector atomic magnetometer, *Phys. Rev. Lett.* **113**, 013001 (2014).  
<sup>15</sup>Y. J. Kim and I. Savukov, Ultra-sensitive magnetic microscopy with an optically pumped magnetometer, *Sci. Rep.* **6**, 24773 (2016).  
<sup>16</sup>H. Zhang, S. Zou, X. Chen, and W. Quan, Parameter modeling analysis and experimental verification on magnetic shielding cylinder of all-optical atomic spin magnetometer, *J. Sens.* **5**, 491746 (2015).  
<sup>17</sup>M. V. Romalis and H. B. Dang, Atomic magnetometers for materials characterization, *Mater. Today*, **14**, 6 (2011).  
<sup>18</sup>E. Boto *et al.*, Moving magnetoencephalography towards real-world applications with a wearable system, *Nature* **555**, 657–661 (2018).

- <sup>19</sup>R.M. Hill *et al.*, Multi-channel whole-head OPM-MEG: Helmet design and a comparison with a conventional system, *NeuroImage* **219**, 116995 (2020).
- <sup>20</sup>M. Rea *et al.*, Precision magnetic field modelling and control for wearable magnetoencephalography, *NeuroImage* **241**, 118401 (2021).
- <sup>21</sup>T.M. Tierney *et al.*, Optically pumped magnetometers: From quantum origins to multi-channel magnetoencephalography, *NeuroImage* **199**, 598–608 (2019).
- <sup>22</sup>A. Borna *et al.*, Non-Invasive Functional-Brain-Imaging with an OPM-based Magnetoencephalography System, *PLOS ONE* **15**, 1–24 (2020).
- <sup>23</sup>H. Eswaran, D Escalona-Vargas, E.H. Bolin, J.D. Wilson, and C.L. Lowery, Fetal magnetocardiography using optically pumped magnetometers: a more adaptable and less expensive alternative?, *Prenat Diagn.* **37**, 193–196 (2017).
- <sup>24</sup>S. Lew, M.S. Hämäläinen, and Y. Okada, Toward noninvasive monitoring of ongoing electrical activity of human uterus and fetal heart and brain, *Clinical Neurophysiology* **128**, 2470–2481 (2017).
- <sup>25</sup>S. Strand, W. Lutter, J.F. Strasburger, V.k. Shah, O. Baffa, and R.T. Wakai, Low-Cost Fetal Magnetocardiography: A Comparison of Superconducting Quantum Interference Device and Optically Pumped Magnetometers, *Journal of the American Heart Association* **8**, 16 (2019).
- <sup>26</sup>A. Mager, Magnetic shielding efficiencies of cylindrical shells with axis parallel to the field, *J. Appl. Phys.* **39**, 1914 (1968).
- <sup>27</sup>S. S. Grabchikov, A. V. Trukhanov, S. V. Trukhanov, I. S. Kazakevich, A. A. Solobay, V. T. Erofeenko, N. A. Vasilenkov, O. S. Volkova, and A. Shakin, Effectiveness of the magnetostatic shielding by the cylindrical shells, *J. Magn. Magn. Mater.* **398**, 49 (2016).
- <sup>28</sup>J. Prat-Camps, C. Navau, D. Chen, and A. Sanchez, Exact analytical demagnetizing factors for long hollow cylinders in transverse field, *IEEE Magn. Lett.* **3**, 0500104 (2012).
- <sup>29</sup>S. Celozzi, R. Araneo, and G. Lovat, Appendix B: Magnetic Shielding, John Wiley & Sons Ltd. (2008).
- <sup>30</sup>A.J. Mäkinen, R. Zetter, J. Iivanainen, K.C.J. Zevenhoven, L. Parkkonen, and R.J. Ilmoniemi, Magnetic field modeling with surface currents. Part I. Implementation and usage of bfieldtools, *J. Appl. Phys* **128**, 063906 (2020).
- <sup>31</sup>R. Zettera, A.J. Mäkinen, J. Iivanainen, K.C.J. Zevenhoven, R.J. Ilmoniemi, and L. Parkkonen, Magnetic field modeling with surface currents. Part II. Implementation and usage of bfieldtools, *J. Appl. Phys* **128**, 063905 (2020).
- <sup>32</sup>M. Packer, P.J. Hobson, N. Holmes, J. Leggett, P. Glover, M.J. Brookes, R. Bowtell, and T.M. Fromhold, Optimal Inverse Design of Magnetic Field Profiles in a Magnetically Shielded Cylinder, *Phys. Rev. Applied* **14**, 054004 (2020).
- <sup>33</sup>M. Packer, P.J. Hobson, N. Holmes, J. Leggett, P. Glover, M.J. Brookes, R. Bowtell, and T.M. Fromhold, Planar Coil Optimization in a Magnetically Shielded Cylinder, *Phys. Rev. Applied* **15**, 064006 (2021).
- <sup>34</sup>C.-Y. Liu, T. Andalib, D. C. M. Ostapchuk, and C. P. Bidinosti, Analytic models of magnetically enclosed spherical and solenoidal coils, *Nucl. Instrum. Methods Phys. Res.* **949**, 162837 (2020).
- <sup>35</sup>R. Lambert and C. Uphoff, Magnetically shielded solenoid with field of high homogeneity, *Rev. Sci. Instrum.* **46**, 3 (1975).
- <sup>36</sup>R. J. Hanson and F. M. Pipkin, Magnetically shielded solenoid with field of high homogeneity, *Rev. Sci. Instrum.* **36**, 2 (1965).
- <sup>37</sup>T. Liu, A. Schnabel, Z. Sun, J. Voigt and L. Li, Approximate expressions for the magnetic field created by circular coils inside a closed cylindrical shield of finite thickness and permeability, *J. Magn. Magn. Mater.* **507**, 0304-8853 (2020).
- <sup>38</sup>H. Tamaki, H. Kita and S. Kobayashi, Multi-objective optimization by genetic algorithms: a review, *Proceedings of IEEE International Conference on Evolutionary Computation* 517-522 (1996).
- <sup>39</sup>H. Tamaki, H. Kita, and S. Kobayashi, Genetic algorithms for modelling and optimisation, *Journal of Computational and Applied Mathematics* **184**, 205-222 (2005).
- <sup>40</sup>K. Deb, *Multi-Objective Optimization Using Evolutionary Algorithms*, Wiley New York (2001).
- <sup>41</sup>K. Deb, A. Pratap, S. Agarwal, and T. Meyarivan A fast and elitist multiobjective genetic algorithm: NSGA-II, *IEEE Transactions on Evolutionary Computation* **6**, 2 182 (2002).
- <sup>42</sup>M. Sakakibara and G. Uehara and Y. Adachi and T. Meguro, Evaluation of Heat Treatment of Mu-Metal Based on Permeability Under Very-Low-Frequency Micromagnetic Fields, *IEEE Transactions on Magnetics* **57**, 2, (2021).
- <sup>43</sup>J. D. Jackson, *Classical electrodynamics* (3rd ed.), Wiley New York (1998).
- <sup>44</sup>P. Hammond, Electric and magnetic images, *Proc. IEE Part C Monogr.* **107**, 306 (1960).
- <sup>45</sup>W.A. Roshen, Effect of finite thickness of magnetic substrate on planar inductors, *IEEE Trans. Magn.* **26**, 270 (1990).
- <sup>46</sup>J. R. Corea, A. M. Flynn, B. Lechene, G. Scott, G. D. Reed, P. J. Shin, M. Lustig, and A. C. Ariasb, Screen-printed flexible MRI receive coils, *Nat. Commun.* **7**, 10839 (2016).
- <sup>47</sup>T. D. Ngo, A. Kashani, G. Imbalzano, K. T. Q. Nguyen, and D. Hui, Additive manufacturing (3D printing): A review of materials, methods, applications and challenges, *Compos. B. Eng.* **143**, 172 (2018).
- <sup>48</sup>M. J. E Golay, Saddle coils for uniform static magnetic field generation in NMR experiments, *Concept Magn. Reson. B* **29B**(1), 9-19 (2016).
- <sup>49</sup>M. J. E Golay, Field homogenizing coils for nuclear spin resonance instrumentation, *Rev Sci Instrum* **29**, 313-315 (1958).
- <sup>50</sup>R. Turner, A target field approach to optimal coil design, *J. Phys. D: Appl. Phys.* **19**, 8 (1986).
- <sup>51</sup>P. M. Morse and H. Feshbach, *Methods of Theoretical Physics*, McGraw-Hill Book Comp. New York (1953).